

1 **SO<sub>2</sub> photolysis as a source for sulfur mass-independent**  
2 **isotope signatures in stratospheric aerosols**

3

4 **A. R. Whitehill<sup>1</sup>, B. Jiang<sup>2</sup>, H. Guo<sup>2</sup>, and S. Ono<sup>1</sup>**

5 [1]{Department of Earth, Atmospheric, and Planetary Sciences, Massachusetts Institute of  
6 Technology, 77 Massachusetts Ave., Cambridge, MA 02139, USA}

7 [2]{Department of Chemistry and Chemical Biology, University of New Mexico,  
8 Albuquerque, NM 87131, USA}

9 Correspondence to: A.R. Whitehill (arwhite@mit.edu)

10

11 **Abstract**

12 Signatures of sulfur isotope mass-independent fractionation(S-MIF) have been observed in  
13 stratospheric sulfate aerosols deposited in polar ice. The S-MIF signatures are thought to be  
14 associated with stratospheric photochemistry following stratospheric volcanic eruptions, but  
15 the exact mechanism responsible for the production and preservation of these signatures is  
16 debated. In order to identify the origin and the mechanism of preservation for these signatures,  
17 a series of laboratory photochemical experiments were carried out to investigate the effect of  
18 temperature and added O<sub>2</sub> on S-MIF produced by the two absorption band systems of  
19 SO<sub>2</sub>:photolysis in the 190 nm to 220 nm region and photoexcitation in the 250 nm to 350 nm  
20 region. The SO<sub>2</sub> photolysis (SO<sub>2</sub>+hv→ SO + O) experiments showed S-MIF signals with  
21 large <sup>34</sup>S/<sup>32</sup>S fractionation, which increases with decreasing temperature. The overall S-MIF  
22 pattern observed for photolysis experiments, including high <sup>34</sup>S/<sup>32</sup>S fractionations, positive  
23 mass-independent anomalies in <sup>33</sup>S, and negative anomalies in <sup>36</sup>S, is consistent with a major  
24 contribution from optical isotopologue screening effects and data for stratospheric sulfate  
25 aerosols. In contrast, SO<sub>2</sub>photoexcitation produced products with positive MIF anomalies in  
26 both <sup>33</sup>S and <sup>36</sup>S that is different from stratospheric aerosols. SO<sub>2</sub> photolysis in the presence of  
27 O<sub>2</sub>produced SO<sub>3</sub> with S-MIF signals, suggesting the transfer of the MIF signals of SO to SO<sub>3</sub>  
28 by the SO + O<sub>2</sub> + M → SO<sub>3</sub> + M reaction. This is supported with energy calculations of  
29 stationary points on the SO<sub>3</sub> potential energy surfaces, which indicate that this reaction occurs

1 slowly on a single adiabatic surface, but that it can occur more rapidly through intersystem  
2 crossing. Based on our experimental results, we estimate a termolecular rate constant on the  
3 order of  $10^{-37}$  cm<sup>6</sup> molecule<sup>-2</sup> s<sup>-1</sup>. This rate can explain the preservation of mass independent  
4 isotope signatures in stratospheric sulfate aerosols and provides a minor, but important,  
5 oxidation pathway for stratospheric SO<sub>2</sub>. The production and preservation of S-MIF signals  
6 in the stratosphere requires a high SO<sub>2</sub> column density to allow for optical isotopologue  
7 screening effects to occur and to generate a large enough signature that it can be preserved. In  
8 addition, the SO<sub>2</sub> plume must reach an altitude of around 20 to 25 km, where SO<sub>2</sub> photolysis  
9 becomes a dominant process. These experiments are the first step towards understanding the  
10 origin of the sulfur isotope anomalies in stratospheric sulfate aerosols.

11

## 12 1 Introduction

13 Explosive volcanic eruptions that inject sulfur dioxide (SO<sub>2</sub>) into the stratosphere can  
14 cause perturbations to the stratospheric sulfur cycle for years following eruptions. The  
15 increase in stratospheric sulfate aerosols associated with injections of SO<sub>2</sub> result in  
16 stratospheric warming and tropospheric cooling, and can also trigger changes in atmospheric  
17 circulation and increases in ozone depletion (Robock, 2000). Perturbations to the stratospheric  
18 sulfur cycle following large volcanic eruptions are recorded as changes in sulfur isotope  
19 ratios, as measured in stratospheric sulfate aerosol samples (Castleman et al., 1974), as well as  
20 in ice core records (Savarino et al., 2003; Baroni et al., 2007).

21 The reaction with OH is the dominant oxidation pathway for SO<sub>2</sub> in the stratosphere:



23 This reaction is followed by:



25 In the presence of H<sub>2</sub>O, SO<sub>3</sub> readily forms sulfuric acid (H<sub>2</sub>SO<sub>4</sub>) via:



27 Ab-initio transition state theory calculations of the isotope effect for OH oxidation (R1)  
28 predict that <sup>34</sup>SO<sub>2</sub> is oxidized 0.9% slower than <sup>32</sup>SO<sub>2</sub> (Tanaka et al., 1994), although  
29 calculations with RRKM theory predicts an inverse isotope effect, in which <sup>34</sup>SO<sub>2</sub> reacts 12%  
30 to 15% faster than <sup>32</sup>SO<sub>2</sub> (Leung et al., 2001). Experimental studies of OH oxidation

1 (R1) showed in an inverse isotope effect, but with a smaller magnitude, with  $^{34}\text{SO}_2$  reacting  
2 about 1% faster than  $^{32}\text{SO}_2$  (Harris et al., 2012). Although the experimentally measured  
3 isotope effect might be sufficient to explain the roughly 2% enrichment in  $\text{H}_2^{34}\text{SO}_4$  relative to  
4  $\text{H}_2^{32}\text{SO}_4$  following the major Mt. Agung (1963) eruption (Castleman et al., 1974), the large  
5 observed isotope effect suggests the possibility of an additional oxidation reaction with larger  
6  $^{34}\text{S}$  fractionations.

7 An additional unexplained observation is the isotope anomalies in  $^{33}\text{S}/^{32}\text{S}$  and  $^{36}\text{S}/^{32}\text{S}$   
8 ratios relative to  $^{34}\text{S}/^{32}\text{S}$  ratios. These signatures of mass-independent fractionation(MIF)  
9 have been observed in ice cores associated with large volcanic eruptions (Savarino et al.,  
10 2003; Baroni et al., 2007, 2008; Lanciki, 2010; Lanciki et al., 2012). Ice core sulfate peaks  
11 are commonly used to reconstruct the impact of past volcanic activity, which is critical to  
12 forcing climate models (Robock, 2000). For several years following large injections of  $\text{SO}_2$   
13 into the stratosphere, stratosphere-derived sulfate can dominate sulfate deposition in ice cores  
14 and, when corrected for background levels, can preserve the sulfur isotopic composition of  
15 stratospheric sulfate aerosols. Experimental studies demonstrate that OH oxidation of  $\text{SO}_2$   
16 (R1) does not produce mass-independent sulfur isotope anomalies (Harris et al., 2012, 2013),  
17 so an additional oxidation mechanism is required to produce the mass-independent sulfur  
18 isotope signatures. Three reactions have been proposed to explain these isotope anomalies:  
19 excited-state photochemistry of  $\text{SO}_2$  in the 250 nm to 350 nm absorption region (Savarino et  
20 al., 2003; Hattori et al., 2013),  $\text{SO}_2$  photolysis in the 190 nm to 220 nm absorption region  
21 (Ono et al., 2013), and  $\text{SO}_3$  photolysis (Pavlov et al., 2005).

22 We present results of laboratory photochemical experiments that support  $\text{SO}_2$   
23 photolysis as the main source for the MIF signatures observed in stratospheric sulfate aerosols  
24 following some large (stratospheric) volcanic eruptions. In particular,  $\text{SO}_2$  photolysis  
25 produces large MIF anomalies, as well as large mass-dependent isotope fractionations  
26 (Masterson et al., 2011; Whitehill and Ono, 2012; Ono et al., 2013) that are consistent with  
27 the isotopic signatures observed in stratospheric sulfate aerosols in ice cores (Ono et al.,  
28 2013).

29 Photolysis of  $\text{SO}_2$  occurs above around 20 to 25 km in the wavelength region of 190  
30 nm to 220 nm, which lies in the spectral window between the Schumann-Runge absorption  
31 edge of oxygen ( $\text{O}_2$ ) and the Hartley bands of ozone ( $\text{O}_3$ ).  $\text{SO}_2$  photolysis produces sulfur  
32 monoxide ( $\text{SO}$ ) and  $\text{O}({}^3\text{P})$  via the following reaction:



2 It is generally accepted that this reaction is followed by rapid oxidation of SO to  $\text{SO}_2$   
3 via (Black et al., 1982; Savarino et al., 2003; Pavlov et al., 2005):



5 Reactions R4 and R5 combine to form a null cycle for sulfur, but catalyze the formation of  
6 odd oxygen (Bekki, 1995). If SO is completely oxidized to  $\text{SO}_2$ , no isotopic signature from  
7  $\text{SO}_2$  photolysis can be preserved (Pavlov et al., 2005).

8 We propose an additional channel where SO is oxidized directly to  $\text{SO}_3$  via the  
9 termolecular reaction:



11 A previous study by Black et al. (1982) showed that the maximum termolecular rate constant  
12 for reaction R6 is  $10^{-36} \text{ cm}^6 \text{ molecule}^{-2} \text{ s}^{-1}$ . This rate is considered too slow to play an  
13 important role for stratospheric chemistry (Black et al., 1982). However, given the large  
14 isotope effects produced during  $\text{SO}_2$  photolysis, even a minor contribution from R6 will  
15 produce a significant signal on the sulfur isotopic composition of stratospheric sulfate  
16 aerosols.

17 We present results from laboratory photochemical experiments that investigate the effect  
18 of temperature and molecular oxygen on the isotope effects produced during  $\text{SO}_2$  photolysis  
19 (190 nm to 220 nm) and  $\text{SO}_2$  photoexcitation (250 nm to 350 nm). Using the results of the  
20 experiments in the presence of molecular oxygen, we calculate a lower bound estimate on the  
21 rate of R6. In addition, our proposal is further supported by ab-initio calculations of  
22 stationary points along the potential energy surfaces (PESs) for the SO oxidation reactions  
23 (R5 and R6). Finally, we present a simple steady state photochemical model to show that the  
24 rate constraints on reaction R6 are sufficient for it to make a significant contribution to the  
25 isotopic signature of stratospheric sulfate aerosols during volcanically perturbed periods.

26 **2 Methods**

27 **2.1 Photochemical reaction set-up**

28 Conditions for all photochemical experiments are listed in Table 1. All experiments were  
29 performed in a cylindrical glass photochemical reaction cell with a pathlength of 15.3 cm and

1 an inner diameter of 5.2 cm (Ono et al., 2013). Temperature-controlled experiments were  
2 performed in a jacketed cell of the same dimensions. The front window of the cell was made  
3 of UV-grade SiO<sub>2</sub> (Corning 7980) with greater than 90% transmittance at wavelengths longer  
4 than 190 nm. The window was sealed to the cell with an o-ring and held in place securely  
5 with a plastic clamp. Temperature-controlled experiments also utilized a second pre-cell (5.3  
6 cm pathlength) attached to the front window of the reaction cell and held under vacuum. The  
7 purpose of the pre-cell was to thermally insulate the front window and prevent condensation  
8 from occurring on the front window during low temperature experiments.

9 A series of mass-flow controllers controlled the flow rate of gases into the cell. Gas entered  
10 the cell through an inlet at the rear of the cell (for temperature cell experiments) or the front of  
11 the cell (for other experiments) and exited the cell through an outlet at the opposite end of the  
12 cell. An 8 cm to 10 cm length of glass tubing packed with glass wool was placed  
13 immediately after the cell exit to trap aerosols formed within the cell. Following the aerosol  
14 trap, the gas was flowed through a proportionating valve to a vacuum pump. A capacitance  
15 manometer placed before the entrance to the cell monitored the pressure within the cell. The  
16 proportionating valve was used to control the pressure within the cell to within 30 Pa of a  
17 setpoint pressure, which was usually 101.3 kPa.

18 Prior to each temperature-controlled experiment, the reaction cell was flushed with  
19 nitrogen(N<sub>2</sub>) for several hours and the chiller was allowed to reach its setpoint temperature  
20 and equilibrate for at least an hour. The temperature of the reaction cell was calibrated  
21 relative to the chiller setpoint temperature on two occasions using a series of K-type  
22 thermocouples suspended within the cell. During calibrations, N<sub>2</sub>(without SO<sub>2</sub>) was flowed  
23 through the cell at a rate of 3.33 cm<sup>3</sup> s<sup>-1</sup> (200 sccm, standard cubic centimeter per minute).  
24 Thermocouples placed at the front and rear of the cell gave consistent measurements to within  
25 5 K, with a higher gradient at lower temperatures. No significant differences were observed  
26 between the two calibrations. Results for the temperature calibration are shown in Figure 1.

27 **2.2 Temperature effect on SO<sub>2</sub> photolysis (190 nm to 220 nm) and**  
28 **photoexcitation (250 nm to 350 nm)**

29 The temperature effect on SO<sub>2</sub> photolysis (190 nm to 220 nm) was tested using the  
30 temperature-controlled reaction cell described in Section 2.1. Experiments were performed in  
31 a nitrogen-flushed glove box to prevent the spectral interference from the Schumann-Runge

1 band of oxygen ( $O_2$ ). A 200 W deuterium ( $D_2$ ) arc lamp (D 200 F, HeraeusNoblelight) was  
2 used as the light source without optical filters. The output from the lamp was collimated  
3 using a fused silica plano-convex lens. 1000 ppm  $SO_2$  (in  $N_2$ ) was flowed through the cell at  
4 a rate of  $3.33\text{ cm}^3\text{ s}^{-1}$  (200 sccm) for all experiments, and pressure within the cell was held  
5 constant at 101.3 kPa, giving an  $SO_2$  partial pressure of 0.10 kPa within the cell.

6 Following photolysis experiments, the cell was removed from the glove box and rinsed well  
7 with dichloromethane to dissolve any elemental sulfur that was formed. The glass wool in the  
8 aerosol trap was also collected and rinsed with dichloromethane. Elemental sulfur was  
9 recrystallized from dichloromethane and converted to silver sulfide using the reduced  
10 chromium chloride method (Whitehill and Ono, 2012; Canfield et al., 1986). Multiple sulfur  
11 isotope ratios were measured as described in Section 2.4.

12 Photoexcitation experiments were performed in a room air atmosphere using a 150 W UV-  
13 enhanced xenon (Xe) arc lamp (Newport Model 6254) housed in a lamp housing (Newport  
14 Model 67005), which focused and collimated the light to a 3.3 cm diameter beam. The light  
15 was passed through a liquid filter (Newport Model 51945) filled with deionized ( $18.2\text{ M}\Omega$ )  
16 water and a 250 nm longpass filter (Asahi Spectra, ZUL0250).

17 Following Whitehill et al. (2013), acetylene ( $C_2H_2$ ) was used to trap triplet excited-state  $SO_2$   
18 ( $^3SO_2$ ). During experiments, 5%  $SO_2$  (in  $N_2$ ), pure  $C_2H_2$  (Atomic Absorption Grade), and  
19 pure  $N_2$  (Ultra High Purity grade) were flowed through the cell continuously at a rate of  $0.67\text{ cm}^3\text{ s}^{-1}$  (40 sccm),  $0.03\text{ cm}^3\text{ s}^{-1}$  (2 sccm), and  $2.63\text{ cm}^3\text{ s}^{-1}$  (158 sccm), respectively. Pressure  
20 in the cell was held constant at 101.3 kPa, giving a total flow rate of  $3.33\text{ cm}^3\text{ s}^{-1}$ , an  $SO_2$   
21 partial pressure of 1.01 kPa, and a  $C_2H_2$  partial pressure of 1.01 kPa within the cell during the  
22 experiments.

24 Following the experiments, the interior walls of the cell and the window were rinsed with  
25 ethanol and water to dissolve any organosulfur products formed. The glass wool in the  
26 aerosol trap was also collected. The organosulfur aerosol products were converted to silver  
27 sulfide using the Raney nickel hydrodesulfurization method of Oduro et al. (2011). Multiple  
28 sulfur isotope ratios were measured as described in Section 2.4.

### 29 **2.3 $SO_2$ photochemistry in the presence of $O_2$**

30 The photochemistry of  $SO_2 + O_2$  with ultraviolet radiation was studied using a reaction cell at  
31 room temperature. The 150 W Xe arc lamp (described in Section 2.2) was used as the light

1 source without the liquid filter. Several experiments were performed with a  $200 \pm 35$  nm  
2 bandpass filter (Model 200-B, Acton Research, Acton, MA), a 250 nm longpass filter (Asahi  
3 Spectra, ZUL0250), or a 280 nm (285 nm cut-on)longpass filter (Newport Model FSR-  
4 WG280) to isolate particular absorption bands of  $\text{SO}_2$ , but most experiments were performed  
5 with the Xe lamp and no filters (Table 1).

6 Following experiments, the cell was rinsed well first with dichloromethane then with water.  
7 Although sulfate was the dominant product, the cell was rinsed well with dichloromethane  
8 first to ensure the removal of elemental sulfur. For two experiments performed with no  
9 oxygen, elemental sulfur was recovered. After rinsing the cell with water,  $5.0 \text{ cm}^3$  of a  $1.0$   
10 mol  $\text{dm}^{-3}$  solution of barium chloride ( $\text{BaCl}_2$ ) was added to the water used to rinse the cell to  
11 precipitate sulfate as barium sulfate. Barium sulfate was rinsed several times with deionized  
12 water and dried. The glass wool inside the aerosol trap was combined with the barium sulfate  
13 and all sulfate was converted to silver sulfide using the method of Forrest and Newman  
14 (1977). Multiple sulfur isotope ratios were measured as described in Section 2.4.

## 15 **2.4 Isotope analysis of photochemical products**

16 Photochemical products were converted to silver sulfide ( $\text{Ag}_2\text{S}$ ).  $\text{Ag}_2\text{S}$  was rinsed well three  
17 to four times with deionized water and then dried completely at 353 K. Dried  $\text{Ag}_2\text{S}$  was  
18 weighed for total yield and about  $8 \mu\text{mol}$  of  $\text{Ag}_2\text{S}$  was weighed into an aluminum foil capsule  
19 for isotope analysis. Capsules were loaded into nickel reaction chambers and reacted under  
20 approximately 7.3 kPa of fluorine gas ( $\text{F}_2$ ) for at least 8 hours at 573 K. The resultant  $\text{SF}_6$   
21 was purified cryogenically and by gas chromatography. Isotope ratios of pure  $\text{SF}_6$  were  
22 measured as  $\text{SF}_5^+$  ions using a Thermo Scientific MAT 253 Isotope Ratio Mass Spectrometer.  
23 For samples where less than  $1.6 \mu\text{mol}$  of  $\text{Ag}_2\text{S}$  was recovered, a microvolume ( $0.4 \text{ cm}^3$   
24 volume) coldfinger was used to concentrate the samples for analysis.

25 Replicate analyses ( $N = 28$ ) of the reference material IAEA-S-1 gave  $2\sigma$  standard  
26 deviations of  $0.26 \text{ \textperthousand}$  for  $\delta^{34}\text{S}$ ,  $0.014 \text{ \textperthousand}$  for  $\Delta^{33}\text{S}$ , and  $0.19 \text{ \textperthousand}$  for  $\Delta^{36}\text{S}$  for standard isotope  
27 ratio mass spectrometry analysis. Microvolume analyses for smaller samples gave  $2\sigma$   
28 standard deviations for replicate analyses of IAEA-S-1 ( $N = 14$ ) of  $0.9 \text{ \textperthousand}$  for  $\delta^{34}\text{S}$ ,  $0.08 \text{ \textperthousand}$  for  
29  $\Delta^{33}\text{S}$ , and  $0.8 \text{ \textperthousand}$  for  $\Delta^{36}\text{S}$ . Replicate experiments performed under identical conditions had  
30 differences larger than the analytical uncertainty, suggesting experimental variability was the  
31 dominant source of uncertainty in our measurements.

1    **2.5 Potential energy surfaces of  $\text{SO} + \text{O}_2 \rightarrow \text{SO}_3 \rightarrow \text{SO}_2 + \text{O}$  reactions**

2    To test the feasibility of reaction R6, ab-initio energy calculations at multiple levels of theory  
3    were performed to search important stationary points on the  $\text{SO}_3$ PESs. The lowest  $\text{SO}(^3\Sigma^-) +$   
4     $\text{O}_2(^3\Sigma_g^-)$  asymptote of the  $\text{SO}_3$  PESs involves three degenerate states, namely the singlet,  
5    triplet, and quintet states. The singlet state corresponds to the ground state of the  $\text{SO}_3$   
6    molecule ( $^1\text{A}_1$ ), but does not dissociate to the ground state products  $\text{SO}_2(^1\text{A}_1) + \text{O}(^3\text{P})$  but to  
7     $\text{SO}_2(^1\text{A}_1) + \text{O}(^1\text{D})$ . The triplet surface corresponds to the ground state products but is  
8    adiabatically associated with a higher energy excited-state (triplet)  $\text{SO}_3$ . The quintet state is  
9    much higher in energy than the other two states except at the  $\text{SO}(^3\Sigma^-) + \text{O}_2(^3\Sigma_g^-)$  asymptote  
10   and will thus not be considered in this study.

11   The B3LYP density functional (Becke, 1988; Lee et al., 1988) was initially used to optimize  
12   each minimum and/or transition state on the singlet and triplet PESs. Single point  
13   calculations at these stationary points were then carried out using an explicitly correlated  
14   version of the unrestricted coupled cluster method with single, double and perturbative triple  
15   excitations (UCCSD(T)-F12a; Knizia et al., 2009).

16   In addition, complete active space self-consistent field (CASSCF) calculations were  
17   performed (Knowles and Werner, 1985, 1988). Multi-reference Rayleigh Schrödinger  
18   perturbation theory of second order (RSPT2 or CASPT2) calculations (Celani and Werner,  
19   2000) were performed based on the CASSCF wavefunctions in order to account for part of  
20   the dynamical correlation. Calculations including the full valence orbitals would involve 24  
21   electrons in 16 orbitals and were not feasible. Instead, the 2s orbital for O and the 3s orbital  
22   for S were closed, resulting in an active space of 16 electrons in 12 orbitals (16e,12o).  
23   Dunning's augmented correlation-consistent polarized valence triplet-zeta (aug-cc-pVTZ)  
24   basis set was used in all cases (Dunning, 1989). B3LYP calculations were performed with  
25   Gaussian09 (Frisch et al., 2009) and the other calculations were performed using  
26   MOLPRO(Werner et al., 2012).

27   **2.6 Definitions**

28   Isotopic results will be presented with conventional  $\delta$  notation, as relative deviations of  
29   isotope ratios with respect to reference sulfur.

$$1 \quad \delta^x S = \frac{\delta^x R_{product}}{\delta^x R_{reference}} - 1 \quad (1)$$

2 where  $x = 33, 34$ , or  $36$  and  $\delta^x R$  is the ratio of  $^xS$  to  $^{32}S$  in the substance. For experimental  
 3 results all isotope ratios will be normalized to the isotope ratios of the initial  $SO_2$ . For natural  
 4 samples (i.e. stratospheric sulfate aerosol samples), the reference is Vienna Canyon Diablo  
 5 Troilite (V-CDT).

6 Mass-independent isotope fractionations in  $^{33}S/^{32}S$  and  $^{36}S/^{32}S$  ratios (relative to  $^{34}S/^{32}S$  ratios)  
 7 will be presented as  $\Delta^{33}S$  and  $\Delta^{36}S$  values, respectively. These are defined as:

$$8 \quad \Delta^{33}S = \frac{(\delta^{33}S + 1)}{(\delta^{34}S + 1)^{0.515}} - 1 \quad (2)$$

9 and

$$10 \quad \Delta^{36}S = \frac{(\delta^{36}S + 1)}{(\delta^{34}S + 1)^{1.90}} - 1 \quad (3)$$

11 Almost all physical, chemical, and biological processes fractionate isotopes mass-dependently  
 12 (i.e.  $\Delta^{33}S$  and  $\Delta^{36}S$  are approximately equal to 0).  $SO_2$  photochemistry, as well as the  
 13 photochemistry of other sulfur gases such as  $CS_2$ , are some of the few exceptions that have  
 14 been shown to produce mass-independent fractionation. Therefore, non-zero  $\Delta^{33}S$  and  $\Delta^{36}S$   
 15 values can be unique tracers of photochemical processes.

### 16 **3 Results**

17 All experiments performed are summarized in Table 1. Results from temperature  
 18 experiments on  $SO_2$  photolysis and  $SO_2$  photoexcitation are given in Tables 2 and 3, whereas  
 19 results from  $SO_2 + O_2$  experiments are presented in Tables 4 and 5. Tables 6, 7, and 8 give  
 20 the results from energy calculations on the PESs of  $SO_3$ .

#### 21 **3.1 Temperature experiments**

22 Results from the temperature experiments (Section 2.2) are shown in Figure 2. The  $SO_2$   
 23 photolysis (190 nm to 220 nm) experiments (Table 2) revealed that the magnitude of the  
 24 isotope effects increase with decreasing temperatures, from 129‰ to 191‰, 5.5‰ to 9.1‰  
 25 and -24.1‰ to -35.8‰, for  $\delta^{34}S$ ,  $\Delta^{33}S$ , and  $\Delta^{36}S$ , respectively. The relationship between  
 26 isotopes (i.e.  $\Delta^{33}S$  versus  $\delta^{34}S$  and  $\Delta^{36}S$  versus  $\Delta^{33}S$ ) did not change significantly as

1 temperature was decreased (0.04 to 0.05 for  $\Delta^{33}\text{S}/\delta^{34}\text{S}$  and -3.9 to -4.6 for  $\Delta^{36}\text{S}/\Delta^{33}\text{S}$ ).  
2 Variability between duplicate experiments also increased at lower temperatures, highlighting  
3 the difficulty of the low temperature experiments and indicating a strong sensitivity to  
4 experimental conditions.

5  $\text{SO}_2$  photoexcitation (250 nm to 350 nm) showdecreasing magnitude  $\Delta^{33}\text{S}$  and  $\Delta^{36}\text{S}$  values at  
6 lower temperatures(22.8‰ to 19.0‰ and 52.5‰ to 46.0‰ for  $\Delta^{33}\text{S}$  and  $\Delta^{36}\text{S}$ , respectively;  
7 Table 3). Even at lower temperatures, the product from  $\text{SO}_2$  photoexcitation experiments  
8 show positive  $\Delta^{33}\text{S}$  and  $\Delta^{36}\text{S}$  values, as shown previously in room-temperature experiments  
9 (Whitehill and Ono, 2012; Whitehill et al., 2013). As discussed previously (Whitehill et al.,  
10 2013), these signatures do not match predictions from isotopologue-specific absorption cross-  
11 sections (Danielache et al., 2012), suggesting an additional isotope effect beyond differences  
12 in the initial excitation for different isotopologues.

### 13 **3.2 Oxygen experiments**

14  $\text{SO}_2$  photolysis and photoexcitation in the presence of molecular oxygen ( $\text{O}_2$ ) produced mass-  
15 independent sulfur isotope signatures in sulfate products (Tables 4 and 5). Isotope ratios of  
16 this product sulfate are shown in Figure 3 and compared with stratospheric sulfate aerosol  
17 data from ice cores (Savarino et al., 2003; Baroni et al., 2007, 2008; Lanciki, 2010; Lanciki et  
18 al., 2012). Strong agreement between the Xe lamp data, 200 nm bandpass (200 BP) data, and  
19 previous  $\text{SO}_2$  photolysis data (Ono et al., 2013) suggest an  $\text{SO}_2$  photolysis source for the  
20 isotope effects during broadband  $\text{SO}_2$  irradiation with the Xe lamp light source.

21 Experiments focusing on the photoexcitation band of  $\text{SO}_2$  using the 250 nm longpass filter  
22 (250 LP) and 280 nm longpass filter (280 LP) display a different isotope signature,  
23 characterized by positive  $\Delta^{33}\text{S}$  and  $\Delta^{36}\text{S}$  values, whereas sulfate from  $\text{SO}_2$  photolysis has  
24 positive  $\Delta^{33}\text{S}$  and negative  $\Delta^{36}\text{S}$  values. This is consistent with previous findings (Whitehill  
25 and Ono, 2012; Whitehill et al., 2013), and demonstrates the MIF in this band region is not  
26 produced by chemistry related to acetylene nor oxygen. However, the magnitude of the sulfur  
27 MIF signatures (i.e.  $\Delta^{33}\text{S}$  and  $\Delta^{36}\text{S}$  values) are considerably smaller than previous experiments  
28 using  $\text{C}_2\text{H}_2$  (Table 3, Whitehill et al., 2013). This suggests that a considerable amountof the  
29 sulfate in the system is being produced by a mass-dependent process, such as  $^*\text{SO}_2 + \text{SO}_2 \rightarrow$   
30  $\text{SO} + \text{SO}_3$  (Whitehill and Ono, 2012). This would dilute the MIF signature.In addition, there  
31 is considerable variability (i.e. a factor of ~2) was observed between the two 250 nm longpass

1 filter experiments, despite identical experimental conditions. The cause of this variability is  
2 uncertain but could relate to the amount of water vapor within the system.

3 **3.3 Potential energy surfaces of SO<sub>3</sub>**

4 Asymptotic energies of SO+O<sub>2</sub> on each PES were compared with the energies obtained by  
5 separate calculations of each species with a certain spin (Table 6). The CASSCF results  
6 correctly produced degenerate energies for the SO+O<sub>2</sub> asymptote on the singlet and triplet  
7 states, which exactly match the sum of the energies of the SO(<sup>3</sup>Σ<sup>-</sup>) and O<sub>2</sub>(<sup>3</sup>Σ<sub>g</sub><sup>-</sup>) species  
8 calculated separately. The CASPT2 results also showed the correct degenerate behavior but  
9 the energies shift slightly from those calculated separately, which presumably arises from the  
10 perturbative treatment in CASPT2. On the other hand, the UCCSD(T)-F12a and B3LYP  
11 results both attribute SO+O<sub>2</sub> on the singlet state to SO(<sup>1</sup>Δ)+O<sub>2</sub>(<sup>1</sup>Δ<sub>g</sub>), and B3LYP even gives a  
12 qualitatively incorrect energy for SO+O<sub>2</sub> on the triplet state, while UCCSD(T)-F12a attributes  
13 the triplet state to SO(<sup>1</sup>Δ)+O<sub>2</sub>(<sup>3</sup>Σ<sub>g</sub><sup>-</sup>). An important conclusion from these data is that one has to  
14 use a multi-reference method if accurate global adiabatic PESs are desired for this system.  
15 Otherwise, the asymptotic behavior can be completely wrong. None of the previous studies  
16 has noticed this, and as a result a single-reference method was always selected (Jou et al.,  
17 1996; Martin, 1999; Goodarzi et al., 2010; Ahmed, 2013). Fortunately, single reference  
18 methods can accurately describe the PES away from the SO+O<sub>2</sub> region; they are capable of  
19 describing several SO<sub>3</sub> isomers and the SO<sub>2</sub>+O product channel reasonably well.

20 Energies for the stationary points computed using multi-reference approaches are reported  
21 relative to that of the SO(<sup>3</sup>Σ<sup>-</sup>)+O<sub>2</sub>(<sup>3</sup>Σ<sub>g</sub><sup>-</sup>) asymptote. However, the active space used in our  
22 CASSCF calculations is not sufficient to provide quantitatively accurate results, but a larger  
23 active space is still computationally infeasible. For single-reference calculations, we chose to  
24 use the UCCSD(T) energies at optimized B3LYP geometries for the stationary points. To  
25 avoid the aforementioned problems in the SO(<sup>3</sup>Σ<sup>-</sup>)+O<sub>2</sub>(<sup>3</sup>Σ<sub>g</sub><sup>-</sup>) asymptote, we have used the  
26 UCCSD(T) energy sum of the two reactants with the correct spins calculated separately, which  
27 has been shown above to be accurate. The sum of these two energies thus provides the  
28 reference for other stationary points on both singlet and triplet PESs. All energies of  
29 stationary points are listed in Tables 7 and 8, and the reaction pathways on both PESs are  
30 shown graphically in Figure 4, using the energies of the UCCSD(T)/B3LYP calculations. It is  
31 seen from Tables 7 and 8 that the experimental derived energy differences (from Chase, 1986)

1 between reactants and products for the  $\text{SO}(^3\Sigma^-) + \text{O}_2(^3\Sigma_g^-) \rightarrow \text{SO}_3(^1\text{A}_1')$  reaction (-411.29 kJ  
2 mole<sup>-1</sup>), the  $\text{SO}(^3\Sigma^-) + \text{O}_2(^3\Sigma_g^-) \rightarrow \text{SO}_2(^1\text{A}_1) + \text{O}(^3\text{P})$  reaction (-54.56 kJ mole<sup>-1</sup>) and the  $\text{SO}(^3\Sigma^-)$   
3  $+ \text{O}_2(^3\Sigma_g^-) \rightarrow \text{SO}_2(^1\text{A}_1) + \text{O}(^1\text{D})$  reaction (135.27 kJ mole<sup>-1</sup>) are reproduced well by the  
4 UCCSD(T)-F12a//B3LYP calculations, while the other methods contain significant errors.

## 5 **4 Discussion**

### 6 **4.1 Origin of mass-independent fractionation during $\text{SO}_2$ photochemistry**

7 The differences in the photophysics and photochemistry between the photolysis region (190  
8 nm to 220 nm) and the photoexcitation region (250 nm to 350 nm)suggest different  
9 mechanisms for MIF formation, as discussed previously (Whitehill and Ono, 2012; Ono et al.,  
10 2013; Whitehill et al., 2013).

11 In the 165 nm to 235 nm wavelength region,  $\text{SO}_2$  photolysis occurs through predissociation  
12 from the bound  $\tilde{C}(^1\text{B}_2)$  state. Near the dissociation threshold of 218.7 nm (Becker et al.,  
13 1995), the quantum yield of photolysis is less than unity, although it increases to greater than  
14 0.99 at wavelengths shorter than 215 nm (Katagiri et al., 1997). In the region where the  
15 quantum yield is close to unity (i.e. less than 215 nm), the isotope effects due to  $\text{SO}_2$   
16 photolysis should be determined entirely by the differences in the absorption cross-sections  
17 between the different isotopologues of  $\text{SO}_2$  (e.g., by isotopologue specific Franck-Condon  
18 coupling; Danielache et al., 2008) and optical screening effects under high  $\text{SO}_2$  column  
19 densities (Lyons, 2007, 2008; Ono et al., 2013). In the narrow spectral region from 215 nm to  
20 218.7 nm, where the quantum yield of photodissociation varies, it is possible that quantum  
21 yield differences between isotopologues could potentially produce additional isotope effects  
22 beyond those predicted from absorption cross-sections. However, in this region,  
23 photodissociation occurs primarily via vibronic mixing of the  $\tilde{C}(^1\text{B}_2)$  state levels with the  
24 dissociative continuum of the electronic ground,  $\tilde{X}(^1\text{A}_1)$  state (Katagiri et al., 1997).Due to the  
25 high density of vibronic levels for the  $\tilde{X}(^1\text{A}_1)$  state, it is unlikely that there will be significant  
26 isotope effects in the coupling strength between the  $\tilde{C}(^1\text{B}_2)$  and  $\tilde{X}(^1\text{A}_1)$  states.Dissociation  
27 occurring through mixing with repulsive singlet and triplet states is expected to be small, as is  
28 the nonadiabatic coupling of the  $\tilde{C}(^1\text{B}_2)$  and  $\tilde{D}(^1\text{A}_1)$  states (Tokue and Nanbu, 2010).

1 For laboratory experiments, the observed isotope effects for SO<sub>2</sub> photolysis is a function not  
2 only of differences in the absorption cross-sections (Danielache et al., 2008) but also a  
3 function of the SO<sub>2</sub> column density. This is because the SO<sub>2</sub> absorption cross-section has  
4 significant fine structure, which causes optical screening effects to occur (Lyons, 2007). This  
5 optical screening effect produces larger isotope effects at higher SO<sub>2</sub> column densities (Ono et  
6 al., 2013). In addition to the above effects, there appears to be a total (or bath gas) pressure  
7 effect on  $\Delta^{33}\text{S}$  values. This manifests as reduced  $\Delta^{33}\text{S}$  values at higher total (i.e. bath gas)  
8 pressures, which is observed with He, SO<sub>2</sub>, and N<sub>2</sub> bath gases (Masterson et al., 2011;  
9 Whitehill and Ono, 2012; Ono et al., 2013). The mechanism responsible for these pressure  
10 effects is still uncertain, but it could suggest that <sup>33</sup>SO<sub>2</sub> has a longer excited-state lifetime  
11 prior to dissociation than the other isotopologues.

12 SO<sub>2</sub>photoexcitation in the 250 nm to 350 nm absorption regionalso produces absorption-based  
13 isotope effects due to differences in cross-sections and self-shielding. In addition, it produces  
14 isotope effects by a completely different mechanism. SO<sub>2</sub>photoexcitation in the 250 nm to  
15 350 nm region occurs by initial excitation into a coupled  $\tilde{A}({}^1\text{A}_2)/\tilde{B}({}^1\text{B}_1)$  singlet excited state  
16 that undergoes intersystem crossing to the photochemically active triplet  $\tilde{a}({}^3\text{B}_1)$  state (Xie et  
17 al., 2013; Lévêque et al., 2014). Unlike SO<sub>2</sub> photolysis, where the quantum yield of reaction  
18 (i.e. photolysis) is near unity, the quantum yield for intersystem crossing between the singlet  
19 and triplet states is highly variable and state-dependent. Due to the relatively low density of  
20 states in the crossing region ( $\tilde{A}({}^1\text{A}_2) \rightarrow \tilde{a}({}^3\text{B}_1)$ ), the branching between quenching to the ground  
21 state and intersystem crossing to the triplet state will be a strong function of isotope  
22 substitution. Whitehill et al. (2013) argue that this isotope selective intersystem crossing as  
23 the origin of part of the isotope effects in photochemical products following  
24 SO<sub>2</sub>photoexcitation in the 250 nm to 350 nm absorption region.

25 Photoexcitation of SO<sub>2</sub> in the presence of O<sub>2</sub> produces sulfate with both positive  $\Delta^{33}\text{S}$  and  
26 positive  $\Delta^{36}\text{S}$  signals, similar to the organic sulfur observed in Whitehill et al. (2013) and the  
27 elemental sulfur in Whitehill and Ono (2012). This suggests that the anomalous isotope  
28 signatures observed from photoexcitation in previous studies are a result of the  
29 photophysicsand photochemistry of excited-state SO<sub>2</sub> rather than the chemistry of subsequent  
30 reactions (i.e., the chemistry with acetylene).Our experimental results show significant  
31 discrepancy with isotope effects predicted by isotopologue-specific absorption cross-sections  
32 (Danielache et al., 2012; Hattori et al., 2013) for the 250 nm to 320 nm region (Whitehill et

1 al., 2013). This is expected if isotope selective intersystem crossing is contributing to the  
2 isotope signals in addition to cross section differences and shielding effects.

3 **4.2 Temperature effects on SO<sub>2</sub> photolysis**

4 Lyons (2007, 2008) presented isotopologue-specific absorption cross-sections for SO<sub>2</sub> in the  
5 190 nm to 220 nm absorption region by shifting the measured <sup>32</sup>SO<sub>2</sub> absorption cross-sections  
6 of Freeman et al.(1984) by an amount based on the calculated isotope shifts of Ran et al.  
7 (2007). It has been unclear whether these absorption cross-sections can correctly predict the  
8 isotope effects due to SO<sub>2</sub> photolysis (Danielache et al. 2008), as they include only isotope  
9 shifts and not other potential differences among isotopologues. Previous comparisons with  
10 experimental data showed significant discrepancies (i.e. a factor of ~2 in  $\delta^{34}\text{S}$  values) between  
11 experimental data and that predicted by the Lyons (2007, 2008) cross-sections (Whitehill and  
12 Ono, 2012; Ono et al., 2013). Such discrepancies were attributed to the difference in  
13 temperature between the Lyons (2007, 2008) cross-sections, which are based on cross-  
14 sections measured at 213 K (Freeman et al., 1984) and the temperature of the experiments  
15 (298 K). Given the new temperature data in the present study, it is possible to compare  
16 calculations based on the Lyons (2007, 2008) cross-sections with temperature-dependent  
17 experimental isotope data. Calculations were performed as described in previous papers  
18 (Whitehill and Ono, 2012; Ono et al., 2013) and are compared to experimental data in Figure  
19 5.

20 Excellent agreement with the Lyons (2007,2008) cross-sections can be seen when the  
21 observed temperature dependence on  $\delta^{34}\text{S}$  are extrapolated back to 213 K. A similar strong  
22 agreement is also seen in the  $\Delta^{36}\text{S}$  values. This new data fills in the major gap between  
23 predictions based on the Lyons (2007, 2008) cross-sections and the room-temperature  
24 experimental data, and provides further support to an optical origin of mass-independent  
25 fractionation during SO<sub>2</sub> photolysis under laboratory conditions (Ono et al., 2013).

26 Despite the strong agreement for  $\delta^{34}\text{S}$  and  $\Delta^{36}\text{S}$  values, the Lyons (2007, 2008) cross-sections  
27 over-predict the magnitude of the mass-independent isotope anomaly in <sup>33</sup>S (i.e.  $\Delta^{33}\text{S}$  values)  
28 when compared with experimental data. There are several possible explanations for this. One  
29 reason is that there are significant differences between the actual cross-sections and those  
30 predicted by shifting the <sup>32</sup>SO<sub>2</sub> cross-sections for <sup>33</sup>SO<sub>2</sub>. Measurements by Danielache et al.  
31 (2008) at room temperature suggest that there are some differences between the isotopologue-

1 specific absorption cross-sections aside from just the spectral shifts accounted for by Lyons  
2 (2007, 2008). A second possibility is that the high total pressure (101.3 kPa, including the N<sub>2</sub>  
3 bath gas) of the experiments caused a decrease in the  $\Delta^{33}\text{S}$  value relative to values observed at  
4 lower total pressures. It has been previously observed (Masterson et al., 2011; Whitehill and  
5 Ono, 2012; Ono et al., 2013) that  $\Delta^{33}\text{S}$  values decrease in the presence of high bath gas  
6 pressures. This pressure quenching effect is most noticeable for  $\Delta^{33}\text{S}$  and does not affect  $\delta^{34}\text{S}$   
7 or  $\Delta^{36}\text{S}$  values as strongly.

8 The Lyons (2007, 2008) cross sections are semi-empirical in that they take the measured  
9 <sup>32</sup>SO<sub>2</sub> cross-sections of Freeman et al. (1984) and shift them using theoretical isotope shifts  
10 predicted by Ran et al. (2007). Although the Lyons (2007, 2008) cross-sections are not  
11 necessarily accurate, the Lyons (2007, 2008) cross sections seem to accurately predict the  
12 isotope effects during SO<sub>2</sub> photolysis under low temperature (ca. 213 K) conditions, such as  
13 those in the stratosphere.

#### 14 **4.3 Constraining the rate of the SO+ O<sub>2</sub> + M reaction using product formation**

15 Our results demonstrate that photolysis of SO<sub>2</sub> in the presence of molecular oxygen (O<sub>2</sub>)  
16 produces large amounts of sulfate with considerable mass-independent sulfur isotope  
17 anomalies. In our experimental system, there are three dominant pathways for SO<sub>3</sub>  
18 formation: OH oxidation of SO<sub>2</sub> (reactions R1 + R2, if water is present), O<sub>2</sub> oxidation of SO  
19 from SO<sub>2</sub> photolysis (reactions R4 + R6), and O oxidation of SO<sub>2</sub> via



21 OH and O oxidation of SO<sub>2</sub> (reactions R1 and R7) are mass dependent (Harris et al., 2012;  
22 Whitehill and Ono, 2012; Ono et al., 2013). However, oxidation of SO via R6 will trap the  
23 isotopic composition of SO as SO<sub>3</sub> and carry the mass-independent sulfur isotope signature  
24 from SO<sub>2</sub> photolysis (R4).

25 We performed a series of experiments at a total pressure of 101.3 kPa, a flow rate of 6.67 cm<sup>3</sup>  
26 s<sup>-1</sup>(400 sccm) and an SO<sub>2</sub> partial pressure of 0.127kPa (Table 4; Figure 6). The partial  
27 pressure of molecular oxygen was varied from 0 kPa to 19.8 kPa (0 % to 19.5% O<sub>2</sub>). In all  
28 experiments, SO<sub>2</sub> was photolyzed via R4. In the experiments with no oxygen, both elemental  
29 sulfur (S<sup>o</sup>) and SO<sub>3</sub> aerosols were formed, with the elemental sulfur (S and related species)  
30 formed from SO via:



2 SO photolysis is expected to be a minor source of S compared to R8. In the absence of  
3 oxygen,  $\text{SO}_3$  is formed primarily via O oxidation of  $\text{SO}_2$  (R7), which is mass dependent (Ono  
4 et al., 2013).

5 At 5.1 kPa O<sub>2</sub> and above, elemental sulfur formation was shut off and SO<sub>3</sub> was the major  
 6 product. Under these conditions, oxidation of SO (to SO<sub>2</sub> or SO<sub>3</sub> via R5 or R6) competes  
 7 with SO disproportionation (R8).

8 By comparing the  $\Delta^{33}\text{S}$  value of elemental sulfur in the absence of  $\text{O}_2$  (0 kPa  $\text{O}_2$ ) with the  
 9  $\Delta^{33}\text{S}$  value of sulfate in the presence of  $\text{O}_2$  (5.1 kPa to 19.8 kPa  $\text{O}_2$ ), it is possible to estimate  
 10 the fraction of sulfate formed through R6. In particular,

$$11 \quad f_{R6} = \frac{\Delta^{33}\text{S}_{\text{sulfate, with O}_2}}{\Delta^{33}\text{S}_{\text{S}^0, \text{no O}_2}} \quad (5)$$

12 where  $f_{R6}$  is the fraction of total  $\text{SO}_3$  formed that comes from reaction R6. Given the product  
 13 yields (Table 4), the time each experiment was run, and the volume of the reaction cell  
 14 (approximately  $325 \text{ cm}^3$ ), the sulfate formation rate per unit volume per unit time can be  
 15 calculated. In the experiments with  $5.1 \text{ kPa}$  to  $19.8 \text{ kPa}$   $\text{O}_2$ , the sulfate formation rates were  
 16 between  $5.3 \times 10^{12} \text{ molecules cm}^{-3} \text{ s}^{-1}$  and  $1.2 \times 10^{13} \text{ molecules cm}^{-3} \text{ s}^{-1}$ . Combining this with  
 17 the  $f_{R6}$  values calculated from equation 5, we can estimate for the rate of sulfate formation  
 18 from reaction R6 under our experimental conditions. This gave a rate for reaction 6 of  
 19  $3.6 \times 10^{12} \text{ molecules cm}^{-3} \text{ s}^{-1}$  to  $6.6 \times 10^{12} \text{ molecules cm}^{-3} \text{ s}^{-1}$ . Assuming R6 is a termolecular  
 20 reaction, the rate for R6 can be written as:

$$21 \quad \text{rate R6} = k_{R6}[\text{SO}][\text{O}_2][\text{M}] \quad (6)$$

22 where  $k_{R6}$  is the termolecular rate constant for reaction R6 and  $[SO]$ ,  $[O_2]$  and  $[M]$  are the  
 23 concentrations of SO, O<sub>2</sub> and total third body gases (M = N<sub>2</sub>, O<sub>2</sub>) in the reaction cell. In  
 24 equation (6), the  $[O_2]$  and  $[M]$  terms are known from the experimental conditions. The  $[SO]$   
 25 term is estimated by assuming a photochemical steady state for SO in the cell. SO production  
 26 via Reaction R4 is balanced by SO destruction via Reactions R5 and R6. This gives us a  
 27 steady state SO concentration of:

$$28 \quad [\text{SO}] = \frac{J_{\text{SO}_2} [\text{SO}_2]}{k_{\text{R5}} [\text{O}_2] + k_{\text{R6}} [\text{O}_2] [\text{M}]} \quad (7)$$

1 where  $J_{SO_2}$  is the photolysis rate constant for R4. This photolysis rate constant was calculated  
2 assuming a spectral irradiance for our 150 W Xe arc lamp of:

3  $F_0 / \text{mW nm}^{-1} = 0.11 \cdot 1.6 \cdot (14 - 9 \cdot \exp(-0.013 \cdot (\lambda / \text{nm} - 200)))$  (8)

4 where  $F_0$  is the spectral irradiance of the xenon lamp at wavelength  $\lambda$  (Ono et al., 2013). This  
5 flux might be modified slightly as a function of the distance between the cell and the lamp,  
6 due to interferences from the absorption of oxygen. However, sensitivity studies performed  
7 here and previously (Whitehill and Ono, 2012) suggest that the effect of the oxygen  
8 absorption on the total  $SO_2$  photolysis rate is minor compared to the uncertainty in the lamp  
9 photon flux. The lamp photon flux data was determined from the manufacturer's data and  
10 uncertainty estimates were not available. Despite this, the function used by Ono et al. (2013)  
11 (Equation 8) was used to obtain an estimate for the total  $SO_2$  photolysis rate.

12 The spectral irradiance of the lamp was used to calculate the photon flux entering the cell,  
13 accounting for absorption of the cell windows from measured transmission data. The  $SO_2$   
14 absorption cross-sections of Manatt and Lane (1993) were used to calculate the photolysis  
15 rate in the cell, accounting for optical screening effects from  $SO_2$  and  $O_2$  within the cell. With  
16 an  $SO_2$  partial pressure of 0.127 kPa, this provided a photolysis rate constant of  $J_{SO_2} = 5.2 \times 10^{-3} \text{ s}^{-1}$ .  
17 The rate constant for reaction R5 is  $k_{R5} = 8.0 \times 10^{-17} \text{ cm}^3 \text{ molecule}^{-1} \text{ s}^{-1}$  (Sander et al.,  
18 2011) at room temperature (298 K). Using these values and equations (6) and (7), the rate  
19 constant for R6 ( $k_{R6}$ ) was calculated iteratively. Calculated rate constants ranged from  $k_{R6} = 7.3 \times 10^{-38} \text{ cm}^6 \text{ molecule}^{-2} \text{ s}^{-1}$  to  $k_{R6} = 1.4 \times 10^{-37} \text{ cm}^6 \text{ molecule}^{-2} \text{ s}^{-1}$ , with an average value of  $k_{R6} = 1.1 \times 10^{-37} \text{ cm}^6 \text{ molecule}^{-2} \text{ s}^{-1}$  (Table 4). This rate estimate is consistent with the upper bound  
20 on  $k_{R6} \leq 1 \times 10^{-36} \text{ cm}^6 \text{ molecule}^{-2} \text{ s}^{-1}$  by Black et al. (1982).

23 The calculated rate constant ( $k_{R6}$ ) appears to decrease at 19.8 kPa  $O_2$  compared with  
24 the calculated rate for lower  $pO_2$  values. It is unclear why this behavior is observed. The  
25 relatively strong agreement for the other conditions strengthens our confidence that the model  
26 is robust.

27 The derived rate constant carries uncertainty due to a number of sources of error in the  
28 rate calculation. One source of error in the calculation is in the spectral irradiance of the  
29 xenon lamp, which was fit from the manufacturer's literature and not directly measured.  
30 Because the spectral irradiance is likely to change over the lamp's lifetime, the actual spectral  
31 irradiance at the time the experiments were performed might be different than the values

1 calculated here. As the spectral irradiance in the high-energy side of the ultraviolet (190 nm  
2 to 220 nm) is likely to decrease over the course of the lamp's lifetime, this makes the  
3 calculated  $\text{SO}_2$  photolysis rate (and resulting  $\text{SO}$  number density) an upper bound. Reducing  
4 the  $\text{SO}_2$  photolysis rate increases the effective rate constant. A second source of error is the  
5 assumption that we trapped 100% of the  $\text{SO}_3$  formed as sulfate. It is possible that some  
6 fraction of the  $\text{SO}_3$  remained in the gas phase and did not condense as aerosol particles. A  
7 third source of error is the assumption that the reaction R6 behaves as a termolecular reaction  
8 despite the high total pressure (101.3 kPa) of the system. It is possible that the reaction is  
9 saturated at (or near) this pressure and is thus behaving as an effective bimolecular reaction.  
10 In any of these three cases, the estimate of the rate constant for reaction R6 would be a lower  
11 bound on the actual termolecular rate constant.

12 It is also important to consider the impact of water vapor within the system. Although  
13 attempts were made to minimize the amount of water vapor in the system, there was almost  
14 certainly some water vapor in the system during our experiments. This is evidenced by  
15 the visible formation of sulfate aerosols from  $\text{SO}_3$  during the experiments. Unfortunately, we  
16 did not have the analytical capability to quantitatively constrain the amount of water vapor in  
17 the system during the experiments. The Zero Air and Nitrogen used as a source of gas to the  
18 cell has a maximum of 3 ppm  $\text{H}_2\text{O}$  (by volume), but there could be additional water absorbed  
19 onto the surfaces of the system while the cell is disassembled. We assume 100% of the  $\text{SO}_3$   
20 was trapped as sulfate, giving a lower bound estimate on the rate of reaction R6.

#### 21 **4.4 Constraining the rate of the $\text{SO} + \text{O}_2 + \text{M}$ reaction using a kinetic model**

22 To further constrain the rate of R6 (the  $\text{SO} + \text{O}_2 + \text{M} \rightarrow \text{SO}_3 + \text{M}$  reaction), we constructed a  
23 kinetic model of the chemistry occurring within the cell. We used the same data and  
24 conditions as Section 4.3, but explicitly modeled the chemistry occurring within the system.  
25  $\text{SO}_2$  photolysis rates were calculated as discussed in Section 4.3, using the cross sections of  
26 Manatt and Lane (1993). Oxygen and ozone photolysis rates were calculated using the cross-  
27 sections Yoshino et al. (1988, 1992) for  $\text{O}_2$  and Molina and Molina (1986) for  $\text{O}_3$ . Quantum  
28 yields for  $\text{O}({}^1\text{D})$  versus  $\text{O}({}^3\text{P})$  formation from  $\text{O}_3$  photolysis were parameterized based on the  
29 recommendation of DeMore et al. (1997). Photolysis rates for  $\text{HO}_2$  and  $\text{H}_2\text{O}_2$  were calculated  
30 using the recommended cross-sections of Sander et al. (2011).  $\text{HO}_2$  photolysis was assumed  
31 to produce  $\text{O}({}^1\text{D})$  and  $\text{OH}$  as products, and  $\text{H}_2\text{O}_2$  photolysis was assumed to produce 2OH.

1 The rate constants and their sources are given in Table 9. Effective second-order rate  
2 constants (calculated assuming  $T = 298$  K and  $[M] = 2.5 \times 10^{19}$  molecule  $\text{cm}^{-3}$ ) were used for  
3 termolecular reactions. Initial guesses were made for the concentration of species within the  
4 system. The system was assumed to be in photochemical steady state and solved iteratively  
5 until convergence. Comparisons were made between the data and the calculations for  $f_{R6}$   
6 values (Equation 5). Simulations were performed with values of  $k_{R6}$  of  $1.0 \times 10^{-37}$   $\text{cm}^6$  molecule $^{-2}$   
7  $\text{s}^{-1}$ ,  $1.0 \times 10^{-36}$   $\text{cm}^6$  molecule $^{-2}$   $\text{s}^{-1}$ , and  $1.0 \times 10^{-35}$   $\text{cm}^6$  molecule $^{-2}$   $\text{s}^{-1}$ . Since the amount of  
8 water vapor in the system was not constrained experimentally, three simulations were  
9 performed, with  $\text{H}_2\text{O}$  concentrations of 0 ppm (by volume), 10 ppm (by volume), and 100  
10 ppm (by volume), which spans a range of reasonable estimates for water vapor concentration  
11 in the system. Although water vapor in the bath gas ( $\text{N}_2$  and  $\text{N}_2/\text{O}_2$ ) are less than 3 ppm (by  
12 volume), additional water could be absorbed onto the inner surfaces of the cell and released  
13 during the experiment. Results for 0 ppm  $\text{H}_2\text{O}$  and 10 ppm  $\text{H}_2\text{O}$  predict rates for reaction R6  
14 on the order of  $10^{-36}$   $\text{cm}^6$  molecule $^{-2}$   $\text{s}^{-1}$ , with predictions for 100 ppm  $\text{H}_2\text{O}$  being slightly  
15 higher.

16 There is a discrepancy between model predictions and the observed experimental behavior.  
17 In particular, lower  $\text{O}_2$  fractions produce higher estimated rates and vice versa. In addition, the  
18 model predicts rates mostly higher than the previous upper bound on the rate calculated by  
19 Black et al. (1982) of  $10^{-36}$   $\text{cm}^6$  molecule $^{-2}$   $\text{s}^{-1}$ . Helium was used as a bath gas for the Black et  
20 al. (1982) experiments, as compared with nitrogen or nitrogen / oxygen used as the bath gas  
21 here. Nitrogen ( $\text{N}_2$ ) and oxygen ( $\text{O}_2$ ) are a more efficient third body quenchers than helium.  
22 Thus, the rate of the termolecular reaction with nitrogen (or nitrogen/oxygen) as a bath gas  
23 could be higher than the maximum constraint suggested by Black et al. (1982). There is also  
24 an order of magnitude discrepancy between the predictions here and those in Section 4.3, with  
25 those in Section 4.3 being an order of magnitude smaller than those in Section 4.4. This could  
26 be based on the assumption that 100% of the  $\text{SO}_3$  was trapped as sulfate in Section 4.3,  
27 whereas the actual amount might be less than that (implying a higher rate than predicted in  
28 Section 4.3). However, the model predicts rate constants within an order of magnitude of  
29 previous constraints from the literature (Black et al., 1982) and Section 4.3. Based on this  
30 work, we estimate the rate of this reaction to be on the order of  $10^{-37}$   $\text{cm}^6$  molecule $^{-2}$   $\text{s}^{-1}$  to  $10^{-$   
31  $36}$   $\text{cm}^6$  molecule $^{-2}$   $\text{s}^{-1}$ . Future work is necessary to better constrain the rate of this reaction.

1    **4.5 Exploring the potential energy surfaces of the SO + O<sub>2</sub> reactions**

2    The experimental evidence presented above suggests the formation of SO<sub>3</sub> via the SO+O<sub>2</sub>  
3    reaction. Our theoretical analysis shows that the singlet PES is associated with the ground  
4    state of the SO<sub>3</sub> molecule, and thus is the primary surface related to the SO(<sup>3</sup>Σ<sup>-</sup>) + O<sub>2</sub>(<sup>3</sup>Σ<sub>g</sub><sup>-</sup>)  
5    →SO<sub>3</sub>(<sup>1</sup>A<sub>1</sub>) reaction (Figure 4). As shown in Table 7, four isomers of SO<sub>3</sub> are located in the  
6    singlet PES. It is predicted that the D<sub>3h</sub>SO<sub>3</sub> isomer is the global minimum, followed by cyclic-  
7    OSOO. There are two shallower wells, denoted as trans-OSOO and cis-OSOO, at the  
8    CASPT2 and UCCSD(T)-F12a levels, but they appear to be energetically higher than the  
9    SO(<sup>3</sup>Σ<sup>-</sup>) + O<sub>2</sub>(<sup>3</sup>Σ<sub>g</sub><sup>-</sup>) asymptote at the B3LYP and CASSCF levels. No barrier was found for  
10   the formation of either trans-OSOO or cis-OSOO, but there is a barrier for the isomerization  
11   and the barrier height depends upon the level of the ab-initio calculation. The rate-  
12   determining barrier for the SO(<sup>3</sup>Σ<sup>-</sup>) + O<sub>2</sub>(<sup>3</sup>Σ<sub>g</sub><sup>-</sup>) →SO<sub>3</sub>(<sup>1</sup>A<sub>1</sub>) reaction is the one connecting  
13   cyclic-OSOO and SO<sub>3</sub>. The lowest barrier height for this reaction (given by CASPT2) is 56.6  
14   kJ mole<sup>-1</sup>. Using the partition function at the B3LYP level, a conventional transition-state  
15   theory rate calculation predicts a pressure-saturated (i.e. effective bimolecular) thermal rate  
16   constant for reaction R6 at 298K of 2.7×10<sup>-24</sup> cm<sup>3</sup> molecule<sup>-1</sup> s<sup>-1</sup>. This is about eight orders of  
17   magnitude lower than the experimental rate constant for reaction R5 (8.0×10<sup>-17</sup> cm<sup>3</sup> molecule<sup>-1</sup>  
18   s<sup>-1</sup>, Sander et al., 2011), and about six orders of magnitude lower than the minimum effective  
19   second-order rate constant for reaction R6 at 101.3 kPa total pressure (about 2.5×10<sup>-18</sup> cm<sup>3</sup>  
20   molecule<sup>-1</sup> s<sup>-1</sup>, calculated assuming  $k_{R6} = 1.0 \times 10^{-37}$  cm<sup>6</sup> molecule<sup>-1</sup> s<sup>-1</sup> and [M] = 2.5×10<sup>19</sup>). We  
21   thus conclude that the SO(<sup>3</sup>Σ<sup>-</sup>) + O<sub>2</sub>(<sup>3</sup>Σ<sub>g</sub><sup>-</sup>) →SO<sub>2</sub>(<sup>1</sup>A<sub>1</sub>) + O(<sup>3</sup>P) reaction cannot occur on the  
22   singlet surface without invoking the spin-forbidden intersystem crossing between the singlet  
23   and triplet surfaces.

24   The triplet PES is very different from the singlet PES with regard to the energy of each SO<sub>3</sub>  
25   isomer (Figure 4; Table 8). The global minimum moves to the cyclic-OSOO isomer, which  
26   has a similar geometry to the singlet (ground) state counterpart but with different bond  
27   lengths. On the other hand, SO<sub>3</sub>(<sup>3</sup>A<sub>1</sub>) becomes highly unfavorable; for example, it is 75.14 kJ  
28   mole<sup>-1</sup> higher than the SO + O<sub>2</sub> reactants at the UCCSD(T)-F12a level. The trans-OSOO  
29   complex remains in a planar geometry, in which the O-S-O-O dihedral angle is 180°;  
30   however, the cis-OSOO complex was found to be out-of-plane, in which the O-S-O-O  
31   dihedral angle is about 74°. We still use “cis-OSOO” to denote this isomer for convenience.  
32   Unlike the singlet PES, trans-OSOO and cis-OSOO share the same transition state for the

1 isomerization to cyclic-OSOO. This process represents the rate-limiting step for the reaction  
2 on the triplet surface. The barrier height is 67.86 kJ mole<sup>-1</sup> at the UCCSD(T)-F12a level,  
3 which is still high. In the adiabatic picture, the  $\text{SO}({}^3\Sigma^-) + \text{O}_2({}^3\Sigma_g^-) \rightarrow \text{SO}_2({}^1\text{A}_1) + \text{O}({}^3\text{P})$   
4 reaction on the triplet PES has a rate constant of  $2.7 \times 10^{-25}$  cm<sup>3</sup> molecule<sup>-1</sup> s<sup>-1</sup> at 298 K,  
5 estimated using transition-state theory. This is still considerably slower than the  
6 experimentally measured rate constant for reaction R5.

7 It is clear that a single PES is unable to reproduce the experimental data for reactions R5 and  
8 R6. In order to explore the possibility of intersystem crossing, two adiabatic minimum energy  
9 pathways on both spin states are shown in Figure 4 and the energies are extracted at the  
10 UCCSD(T)-F12a//B3LYP level. There are several places that the two PESs cross each other,  
11 and a spin flip could happen in the region near the cyclic-OSOO isomer due to the fact that  
12 this isomer on both PESs has nearly the same energy. A possible non-adiabatic reaction  
13 pathway is depicted in Figure 4 by the green solid lines connecting every two stationary  
14 points. Specifically, for the  $\text{SO}({}^3\Sigma^-) + \text{O}_2({}^3\Sigma_g^-) \rightarrow \text{SO}_3({}^1\text{A}_1')$  reaction, the two reactants first  
15 approach each other to form cyclic-OSOO on the singlet PES, and jump to the triplet PES to  
16 avoid the high barrier region, followed by back transition to the singlet state to form the  $\text{SO}_3$   
17 product. For the  $\text{SO}({}^3\Sigma^-) + \text{O}_2({}^3\Sigma_g^-) \rightarrow \text{SO}_2({}^1\text{A}_1) + \text{O}({}^3\text{P})$  reaction, the intermediate cyclic-  
18 OSOO may be generated on the singlet PES, followed by intersystem crossing from the  
19 singlet to triplet surface and then reach the products without overcoming a high barrier.  
20 Indeed, several different mechanisms introducing the intersystem crossing have been  
21 proposed by other authors for the  $\text{SO}_3 \rightarrow \text{SO}_2 + \text{O}$  reaction (Davis, 1974; Westenberg and  
22 Dehaas, 1975; Astholz et al., 1979), thanks to the relatively large spin-orbit coupling of the  
23 heavy sulfur. The barrier associated with the intersystem crossing pathway seems to be  
24 consistent with the fast rate of R5, and supports the facile formation of  $\text{SO}_3$ .

25 Unfortunately, rate constants involving the intersystem crossing cannot be readily determined  
26 from the current calculations. Global PESs for both spin states and the coupling between them  
27 would be required for a complete calculation. Such a goal can only be achieved by a multi-  
28 reference method or configuration interaction method, which is infeasible at the current level.  
29 On-the-fly surface hopping calculations would present an alternative method to derive rate  
30 constants without the need for global potential energy surfaces and should be pursued in  
31 future work.

1    **4.6 Contribution of the SO + O<sub>2</sub> + M reaction to sulfate formation in the**  
 2    **stratosphere**

3    To determine the significance of the reaction R6 to sulfate formation in the stratosphere, we  
 4    compared the rate of sulfate formation via R6 to that formed via OH oxidation of SO<sub>2</sub>  
 5    (reaction R1) and O oxidation of SO<sub>2</sub> (reaction R7) under a select set of atmospheric  
 6    conditions. We assumed an atmospheric temperature and pressure profile of the U.S. Standard  
 7    Atmosphere 1976 (COESA, 1976) and noon-time O, OH, and O<sub>3</sub> concentrations given by  
 8    DeMore et al. (1997). Spectral photon flux in the 180 nm to 220 nm region was calculated as  
 9    a function of altitude for a solar zenith angle of 40° by assuming the spectral photon irradiance  
 10   of Rottman et al. (2006) at the top of the atmosphere and O<sub>2</sub>, O<sub>3</sub>, and CO<sub>2</sub> being the dominant  
 11   absorbers. Absorption cross-sections of O<sub>2</sub> (Yoshino et al., 1988, 1992), O<sub>3</sub> (Molina and  
 12   Molina, 1986), and CO<sub>2</sub> (Shemansky, 1972) were used with concentration and column density  
 13   data for the species to calculate the transmission of the atmosphere to radiation in the 180 nm  
 14   to 220 nm absorption region at different altitudes. SO<sub>2</sub> photolysis rate constants ( $J_{SO_2}$ ) were  
 15   calculated as a function of altitude using the calculated spectral photon fluxes and the SO<sub>2</sub>  
 16   absorption cross-sections of Manatt and Lane (1993).

17   The lifetime of SO with respect to oxidation by O<sub>2</sub> (i.e. R5 and R6) is relatively short (on the  
 18   order of seconds), so SO and SO<sub>2</sub> were assumed to be in photochemical steady state, i.e.

$$19 \quad \frac{[SO]}{[SO_2]} = \frac{J_{SO_2}}{k_{R5}[O_2] + k_{R6}[O_2][M]} \quad (9)$$

20   The rate constant  $k_{R5}$  was calculated as a function of altitude (i.e. temperature) based on the  
 21   recommendations of Sander et al. (2011).  $k_{R6}$  was varied between  $1.0 \times 10^{-37}$  cm<sup>6</sup> molecule<sup>-2</sup> s<sup>-1</sup>  
 22   and  $1.0 \times 10^{-36}$  cm<sup>6</sup> molecule<sup>-2</sup> s<sup>-1</sup> to encompass the order of magnitude rate estimates from  
 23   Section 4.3 and 4.4. SO oxidation by other oxidants (O<sub>3</sub>, O, NO<sub>3</sub>, etc.) was assumed to be  
 24   minor compared to oxidation by O<sub>2</sub> given the minor concentration of most of these species  
 25   compared with that of O<sub>2</sub>. Using the [SO] to [SO<sub>2</sub>] ratio, the rates of R1, R7, and R6 can be  
 26   compared. Assuming these three reactions are the dominant source of SO<sub>3</sub> (and subsequently  
 27   sulfate) in the stratosphere, the fraction of sulfate from reaction R6 ( $f_{SO}$ ) can be calculated as:

$$28 \quad f_{SO} = \frac{\frac{[SO]}{[SO_2]} \cdot k_{R6}[O_2][M]}{k_{SO_2+OH}[OH] + k_{SO_2+O}[O] + \frac{[SO]}{[SO_2]} \cdot k_{R6}[O_2][M]} \quad (10)$$

1 The rate constants  $k_{\text{SO}_2+\text{OH}}$  and  $k_{\text{SO}_2+\text{O}}$  are the effective bimolecular rate constants for reactions  
2 R1 and R7, as recommended by Sander et al. (2011).  $f_{\text{SO}}$  values were calculated for a 40°  
3 solar zenith angle (local noon at 40°N latitude and a 0° solar declination angle) and are shown  
4 in Figure 8. Given that SO, OH, and O(<sup>3</sup>P) are all formed as a result of photochemistry, they  
5 should have similar daily cycles. As a result, the  $f_{\text{SO}}$  values calculated for local noon should  
6 be similar to daily average  $f_{\text{SO}}$  values.

7 As seen in Figure 8, the lower estimate for  $k_{\text{R6}}$  ( $1.0 \times 10^{-37}$  cm<sup>6</sup> molecule<sup>-2</sup> s<sup>-1</sup>) gives 4% to 10%  
8 of sulfate from R6 between 25 km and 50 km altitude. A faster estimate for  $k_{\text{R6}}$  of  $2.0 \times 10^{-37}$   
9 cm<sup>6</sup> molecule<sup>-2</sup> s<sup>-1</sup> gives 8% to 18% of sulfate from R6 between 25 km and 50 km altitude.  
10 The upper bound estimate for the rate ( $k_{\text{R6}} = 1.0 \times 10^{-36}$  cm<sup>6</sup> molecule<sup>-2</sup> s<sup>-1</sup>, from Black et al.,  
11 1982) suggests that over 45% of sulfate could be coming from R6 between 31 km and 34 km  
12 altitude and is probably unrealistic. The contribution from R6 depends upon the amount of  
13 photons available for SO<sub>2</sub> photolysis, which increases with altitude because of less absorption  
14 by Schuman-Runge band of O<sub>2</sub> and the Hartley bands of O<sub>3</sub>. The rate of R6 decreases at  
15 higher altitude as total number density decrease. The maximum  $f_{\text{SO}}$  value, thus, is between 30  
16 and 35 km (Figure 8).

17 Some insight into the rate can be obtained from SO<sub>2</sub> lifetimes in the stratosphere. Following  
18 the Mt. Pinatubo (1991) eruption, the Total Ozone Mapping Spectrometer (TOMS) data  
19 (Bluth et al., 1992) and Microwave Limb Sounder (MLS) data (Read et al., 1993) were used  
20 to estimate an e-folding time of 33 days to 35 days for SO<sub>2</sub> in the stratosphere. A later  
21 reanalysis of the TOMS data and TIROS Optical Vertical Sounder (TOVS) data (Guo et al.,  
22 2004) reduced this value to 25 days. Bekki and Pyle (1994) modeled the SO<sub>2</sub> decay following  
23 the Mt. Pinatubo eruption, considering R1 as the only sink of SO<sub>2</sub> in the stratosphere. Their  
24 modeled decay times for SO<sub>2</sub> (40 days) are considerably longer than the measured value of 25  
25 days. Bekki and Pyle (1994) attributed this to uncertainties in the OH number densities. The  
26 discrepancy, however, could be explained in part by SO<sub>2</sub> photolysis followed by R6. Inclusion  
27 of the SO<sub>2</sub> photolysis sink would decrease the lifetimes for SO<sub>2</sub> above around 25 km. The  
28 presence of this reaction would also suggest that OH concentrations estimated by Read et al.  
29 (1993) based on SO<sub>2</sub> lifetimes might overestimate OH concentrations above around 25 km  
30 altitude.

31 SO<sub>2</sub> photolysis is self-limiting, as SO<sub>2</sub> photolysis near the top of the volcanic SO<sub>2</sub> plume  
32 absorbs ultraviolet radiation in the range that SO<sub>2</sub> photolysis occurs. As a result, SO<sub>2</sub>

1 photolysis lower in the eruption cloud is reduced and depends upon the overlying SO<sub>2</sub> column  
2 density. This would potentially reduce the significance of R6 under heavy SO<sub>2</sub> loading.

3 Optical shielding effects increase the magnitude of the isotope effect from SO<sub>2</sub> photolysis  
4 under high SO<sub>2</sub> column densities (Lyons et al., 2007; Ono et al., 2013). Thus, the isotope  
5 fractionation occurring in a volcanic cloud is a tradeoff between larger fractionations but  
6 lower photolysis rates at higher column densities versus smaller fractionations but higher  
7 photolysis rates at lower column densities. Although the instantaneous fractionation factors  
8 can be estimated using our results and cross section by Lyons (2007, 2008), the temporal  
9 evolution of isotope signatures of sulfate aerosol will require a model that accurately  
10 incorporates both chemistry and dynamics of stratosphere.

11 Given the large signal produced by SO<sub>2</sub> photolysis, over 100‰ and 10‰ for  $\delta^{34}\text{S}$  and  $\Delta^{33}\text{S}$   
12 values, respectively (Whitehill and Ono, 2012; Ono et al., 2013), even a 10% contribution  
13 from reaction R5 could make a substantial contribution to the isotope signature of sulfate  
14 formed above circa 25 km altitude. Given the strong similarity in the isotopic signature of  
15 stratospheric sulfate aerosols from volcanic eruptions and those produced during SO<sub>2</sub>  
16 photolysis (Figure 3), it is likely that SO<sub>2</sub> photolysis plays an important role in the sulfur  
17 isotope budget of stratospheric sulfate aerosols. The initial sulfate formed from SO<sub>2</sub>  
18 photolysis (followed by R6) will contain positive  $\delta^{34}\text{S}$  and  $\Delta^{33}\text{S}$  values and negative  $\Delta^{36}\text{S}$   
19 values. Over time, due to mass balance, the residual SO<sub>2</sub> will obtain negative  $\delta^{34}\text{S}$  and  $\Delta^{33}\text{S}$   
20 values and positive  $\Delta^{36}\text{S}$  values. This explains the temporal evolution of the isotopic  
21 signatures observed in aerosol samples (for  $\delta^{34}\text{S}$ , Castleman et al., 1974) and ice cores (Baroni  
22 et al., 2007), which goes from positive  $\delta^{34}\text{S}$  and  $\Delta^{33}\text{S}$  values shortly after an eruption to  
23 negative values as time progresses.

24

#### 25 **4.7 Insignificance of excited-state photochemistry of SO<sub>2</sub> in the stratosphere**

26 It has been suggested previously (Savarino et al., 2003; Hattori et al., 2013) that excited-state  
27 photochemistry of SO<sub>2</sub> in the 250 nm to 350 nm absorption region (i.e. the  $\tilde{A}({}^1\text{A}_2)/\tilde{B}({}^1\text{B}_1)$   
28 states) might be the dominant source of the sulfur isotope ratios in stratospheric sulfate  
29 aerosols. Previous results (Whitehill and Ono, 2012; Whitehill et al., 2013) have  
30 demonstrated that SO<sub>2</sub> photoexcitation in this region produces mass-independent sulfur  
31 isotope signatures with positive  $\Delta^{36}\text{S}/\Delta^{33}\text{S}$  ratios, as opposed to the negative  $\Delta^{36}\text{S}/\Delta^{33}\text{S}$  ratios

1 measured for stratospheric sulfate aerosols. This study further demonstrates that  
2  $\text{SO}_2$ photoexcitation in the 250 nm to 350 nm absorption region produces positive  $\Delta^{36}\text{S}/\Delta^{33}\text{S}$   
3 ratios, even at temperatures approaching stratospheric temperatures. Our previous  
4 experiments (Whitehill and Ono, 2012; Whitehill et al., 2013) have been questioned as being  
5 inapplicable to the modern atmosphere (Hattori et al., 2013) due to the experimental  
6 conditions (i.e. the addition of  $\text{C}_2\text{H}_2$  to trap triplet-state  $\text{SO}_2$ ). In the present study, we tested  
7  $\text{SO}_2$ photoexcitation with two different longpass filters (250 nm longpass filter and 280 nm  
8 longpass filter) in a  $\text{N}_2/\text{O}_2$  bath gas. In all cases, we produced sulfate products with positive  
9  $\Delta^{36}\text{S}/\Delta^{33}\text{S}$  ratios. Therefore, our experiments do not provide support for  $\text{SO}_2$ photoexcitation  
10 as the dominant source of the isotope anomalies in modern atmospheric samples.

11 However, contribution from both absorption bands to the isotope effects observed in  
12 stratospheric sulfate aerosols is possible and should be considered further. Despite the strong  
13 correspondence between  $\Delta^{36}\text{S}/\Delta^{33}\text{S}$  ratios in our photolysis experiments and stratospheric  
14 sulfate aerosol samples (Figure 3), the stratospheric sulfate aerosol samples produces a  
15 slightly shallower (less negative)  $\Delta^{36}\text{S}/\Delta^{33}\text{S}$  slope than the majority of our experimental  
16 samples. This could be due in part to the effect of pressure on  $\Delta^{36}\text{S}/\Delta^{33}\text{S}$  ratios (Masterson et  
17 al., 2011), as the one experiment performed at 7.7 kPa total pressure (Table 5) produced a  
18  $\Delta^{36}\text{S}/\Delta^{33}\text{S}$  more similar to the stratospheric sulfate aerosol samples than the experiments  
19 performed at 101.3 kPa total pressure. It could also be due, however, to mixing between the  
20 negative  $\Delta^{36}\text{S}/\Delta^{33}\text{S}$  signatures from  $\text{SO}_2$  photolysis and the positive  $\Delta^{36}\text{S}/\Delta^{33}\text{S}$  signatures from  
21  $\text{SO}_2$ photoexcitation. It is critical that future experiments further explore the isotope effects  
22 within these two absorption regions. However, it is also clear that  $\text{SO}_2$ photoexcitation alone  
23 is not likely to be responsible for the isotope signatures and that  $\text{SO}_2$  photolysis is necessary  
24 as well.

## 25 **4.8 Caveats for Experimental Studies**

26 There are a number of difficulties with directly applying photochemical results from  
27 laboratory studies to processes occurring in the natural environment. One issue is the  
28 difference between the spectral photon flux of the  $\text{Xe}$  and  $\text{D}_2$  arc lamps as compared with the  
29 solar spectrum. Comparisons of data from different light sources ( $\text{Xe}$  versus  $\text{D}_2$  lamps) were  
30 made previously in static photochemical experiments (Whitehill and Ono, 2012) and showed  
31 minor differences depending upon the light source. However, despite the large differences in  
32 the spectral photon flux between the  $\text{Xe}$  and  $\text{D}_2$  light sources, the patterns in the isotope

1 fractionation (i.e.  $\delta^{34}\text{S}$  versus  $\Delta^{33}\text{S}$  versus  $\Delta^{36}\text{S}$ ) are similar. Both the Xe and D<sub>2</sub> light sources  
2 are broadband, unstructured light sources in the 180 nm to 220 nm absorption region, where  
3 SO<sub>2</sub> photolysis occurs. The solar spectrum, although also broadband, has considerably more  
4 fine structure in the spectrum, due to absorption by other gases such as O<sub>2</sub>. As demonstrated  
5 in early SO<sub>2</sub> photolysis experiments (Farquhar et al. 2001), highly structured light sources  
6 (such as laser light sources) can cause anomalous isotope effects different from those  
7 observed in a broadband regime (Whitehill and Ono, 2012).

8 Unfortunately, the currently available measured absorption cross-sections (Danielache  
9 et al. 2008) do not reproduce the results of photochemical experiments (Whiteihll and Ono,  
10 2012). As shown by Ueno et al. (2009), they predict negative  $\Delta^{33}\text{S}$  values from SO<sub>2</sub>  
11 photolysis under reasonable atmospheric conditions. Photochemical experiments show  
12 positive  $\Delta^{33}\text{S}$  values near zero (except in the self-shielding regime; Ono et al., 2013) under  
13 similar conditions. It is also important to note that the magnitude of uncertainties in the cross-  
14 section measurements (on the percent level) are too large to be considered quantitative for that  
15 of mass-independent fractionation observed in these reactions. Future, higher-precision and  
16 higher resolution cross-section measurements should resolve some of these discrepancies and  
17 allow for stratospheric fractionations under solar spectral conditions to be modeled. In the  
18 absence of this data, however, experiments using solar-like spectra (i.e. Xe arc lamp) can  
19 provide a first order constraint on the types of isotope fractionations expected under a solar  
20 regime.

21 Another major issue with the experiments that was discussed above is the poor control  
22 in the experiments over the amount of water in the system. Due to the fact that experiments  
23 were performed at room temperature rather than at vacuum, it is difficult to put definitive  
24 constraints on the amount of water present in the system. Although attempts were made to  
25 flush the systems with nitrogen (< 3 ppb H<sub>2</sub>O) prior to each experiment, water could be  
26 adsorbed onto the surfaces of the system. The presence of water will cause HO<sub>x</sub> chemistry to  
27 occur and open up an additional (mass-dependent, Harris et al. 2012) channel for sulfate  
28 formation. The amount of water in the system also affects the amount of SO<sub>3</sub> that ends up as  
29 sulfate aerosols. This is particularly an issue when attempting to estimate the rate of reactions  
30 in the system (Section 4.3 and 4.4). Differences in the amount of water within the system  
31 during different experiments could explain some of the isotopic variability between replicate  
32 experiments (Tables 4 and 5). Photoexcitation (250 nm to 350 nm) experiments performed in

1 an identical photochemical system but with the addition of acetylene ( $C_2H_2$ ) are not strongly  
2 affected by the presence of trace amounts of water in the system, and showed considerably  
3 better isotopic reproducibility (Whitehill et al. 2013; Table 3) than  $SO_2$  photolysis  
4 experiments (Ono et al., 2013; Tables 2, 4, and 5). This suggests that variability in trace  
5 amounts of water present in the system could have a significant affect on the isotopic  
6 signatures during  $SO_2$  photolysis, and that water vapor should be carefully controlled in future  
7 experiments.

8

9 **4.9 Production and preservation of mass-independent sulfur isotope  
10 signatures in ice cores**

11 The results presented in this paper can explain the production and preservation of mass-  
12 independent sulfur isotope signatures in the modern atmosphere. Large volcanic eruptions,  
13 such as Pinatubo (1991) and Agung (1963) inject large amounts of  $SO_2$  into the stratosphere.  
14 Both direct injection into higher altitudes (i.e. above around 20 to 25 km) or stratospheric  
15 transport of the  $SO_2$  plume can bring  $SO_2$  to a sufficient altitude for  $SO_2$  photolysis to occur.  
16 The process of  $SO_2$  photolysis produces large mass-independent sulfur isotope signatures in  
17 the  $SO$  products, particularly when there is high  $SO_2$  loading (and thus optical screening  
18 effects). Reaction of  $SO$  with  $O_2$  to produce  $SO_3$  (via R6) provides a pathway for the isotopic  
19 signature of  $SO$  to be preserved as  $SO_3$ , which can subsequently form sulfate aerosols. Some  
20 portion of the sulfate aerosols containing the mass-independent sulfur isotope signatures are  
21 transported to polar regions, where they can be deposited in polar precipitation and preserved  
22 in ice core records. A schematic illustration of the process is shown in Figure 9.

23 Some eruptions, despite their stratospheric influence, produce sulfate peaks in ice core records  
24 but do not contain mass-independent sulfur isotope signatures. Such eruptions include Cerro  
25 Hudson (1991, Savarino et al., 2003) and Laki (1783, Lanciki et al., 2012). Schmidt et al.  
26 (2012) discussed this issue previously and concluded that the Laki aerosols deposited in the  
27 Greenland ice cores were predominantly upper tropospheric or lower stratospheric in  
28 origin. Estimates for the height of the Laki (1783) eruption plume are only 15 km (Thordarson  
29 and Self, 2003), which penetrates the stratosphere but is not sufficiently high for  $SO_2$   
30 photolysis to be a dominant process (Schmidt et al., 2012). Due to the higher latitude of the  
31 eruption, transport processes are unlikely to bring the eruption plume to a sufficient altitude

1 (25 km) for  $\text{SO}_2$  photolysis to occur. Thus, despite the stratospheric influence of the Laki  
2 eruption, mass-independent sulfur isotope signatures in the preserved aerosols would not be  
3 expected. The situation is similar for the Cerro Hudson (1991) eruption, which had an  
4 injection height of 11 km to 16 km (Schoeberl et al., 1993). Again, given the high latitude of  
5 the eruption, transport processes are likely insufficient to bring the plume to a sufficient  
6 altitude for  $\text{SO}_2$  photolysis to becomea dominant process.

7 Low-latitude eruptions such as Pinatubo (1991) might behave differently. Although the initial  
8 injection of the Pinatubo eruption was probably localized below 25 km, the evolution of the  
9 plume resulted in the plume reaching altitudes of 30 km or higher (Gobi et al., 1992),  
10 sufficient altitudes for  $\text{SO}_2$  photolysis to play a role in the oxidation to sulfate. The largest  
11 mass-independent sulfur isotope signatures (with  $\Delta^{33}\text{S} > 1\text{\textperthousand}$ ) observed to date are from the  
12 Samalas (1257, Lavigne et al., 2013) eruption (Lanciki et al., 2012). Evidence suggests the  
13 eruption plume from this reaction reached a minimum of 34 km altitude, with a likely  
14 estimate being 43 km altitude (Lavigne et al., 2013). At this altitude,  $\text{SO}_2$  photolysis would  
15 become a dominant process, and could explain why the signature from this eruption is  
16 significantly larger that the other eruptions. Thus,  $\text{SO}_2$  photolysis, followed by  $\text{SO}$  oxidation  
17 to  $\text{SO}_3$  (via R6), presents a consistent mechanism through which mass-independent sulfur  
18 isotope signatures can be produced and preserved in the modern, oxygenated stratosphere.

19

## 20 **5 Conclusions**

21 Laboratory photochemical experiments were carried out to investigate the production of  
22 mass-independent sulfur isotope effects under stratospheric conditions. For  $\text{SO}_2$  photolysis in  
23 the 190 nm to 220 nm region, the magnitude of the mass-independent isotope signature  
24 increases with decreasing temperature. The isotope systematics, in particular  $\delta^{34}\text{S}$  and  $\Delta^{36}\text{S}$   
25 values, show excellent agreement with an optical self-screening model basedon synthetic  
26 absorption cross sections (Lyons, 2007).  $\text{SO}_2$ photoextciation experiments show similar  
27 signatures to previous experimental studies (Whitehill and Ono, 2012; Whitehill et al., 2013),  
28 with positive  $\Delta^{33}\text{S}$  and  $\Delta^{36}\text{S}$  values, but that differ significantly from expectations based on  
29 absorption cross sections (Danielache et al., 2012).

30 The  $\text{SO}_3$  (recovered as sulfate) products from  $\text{SO}_2$  photolysis in the presence of molecular  
31 oxygen carry mass-independent sulfur isotope signatures, suggesting a pathway for the direct

1 oxidation of SO to SO<sub>3</sub>. We hypothesize the SO + O<sub>2</sub> + M → SO<sub>3</sub> + M reaction (R6) and  
2 estimate the termolecular rate constant of the reaction to be on the order of 10<sup>-37</sup> cm<sup>6</sup>  
3 molecules<sup>-2</sup> s<sup>-1</sup> or faster. This is consistent with previous constraints on the maximum rate of  
4 this reaction (Black et al., 1982).

5 We calculated the energies of stationary points on the singlet and triplet potential energy  
6 surfaces of SO<sub>3</sub> that are associated with the SO(<sup>3</sup>Σ<sup>-</sup>)+O<sub>2</sub>(<sup>3</sup>Σ<sub>g</sub><sup>-</sup>) asymptote at several different  
7 levels of theory and show that reaction R6 is theoretically possible via intersystem crossing  
8 between the singlet and triplet surfaces. We also show that the measured rate for SO + O<sub>2</sub> +  
9 → SO<sub>2</sub> + O reaction (R5) also requires intersystem crossing between the singlet and triplet  
10 surfaces.

11 Depending on the rate of R6, we predict that on the order of 10% of sulfate above 25 km  
12 altitude could be derived from the SO + O<sub>2</sub> + M channel. Given the large isotope  
13 fractionations produced during SO<sub>2</sub> photolysis, our model can explain the source and  
14 preservation mechanism of mass-independent sulfur isotope signatures measured in  
15 stratospheric sulfate aerosols in polar ice samples. Furthermore, our model explains the  
16 temporal evolution of δ<sup>34</sup>S and Δ<sup>33</sup>S values following major volcanic eruptions, and constrains  
17 the maximum altitude of the plume to above 20 to 25 km when non-zero Δ<sup>33</sup>S values are  
18 observed.

19 **Acknowledgements**

20 The authors would like to thank William J. Olszewski for his assistance in sulfur isotope  
21 analysis, and support from NASA Exobiology (NNX10AR85G to S.O., and 11-EXO11-0107  
22 to H.G.) and NSF FESD (Award 1338810 to S.O.). The authors would like to thank editor  
23 Thomas Röckmann and reviewers Matthew Johnson and Joel Savarino for their comments.

24

1    **References**

2    Ahmed, M. M.: Theoretical studies on the ground and excited states of SO<sub>3</sub> triatomic  
3    molecule, *Chem. Sci. Trans.*, 2, 781-796, doi: 10.7598/cst2013.515, 2013.

4    Astholz, D. C., Glanzer, K., and Troe, J.: The spin-forbidden dissociation-recombination  
5    reaction SO<sub>3</sub>→ SO<sub>2</sub>+O, *J. Chem. Phys.*, 70, 2409-2413, doi:10.1063/1.437751, 1979.

6    Baroni, M., Thiemens, M. H., Delmas, R. J., and Savarino, J.: Mass-independent sulfur  
7    isotopic compositions in stratospheric volcanic eruptions, *Science*, 315, 84-87  
8    doi:10.1126/science.1131754, 2007.

9    Baroni, M., Savarino, J., Cole-Dai, J., Rai, V. K., and Thiemens, M. H.: Anomalous sulfur  
10   isotope compositions of volcanic sulfate over the last millennium in Antarctic ice cores, *J.*  
11   *Geophys. Res. Atmos.*, 113, D20112, doi:10.1029/2008JD010185, 2008.

12   Becke, A. D., Density-functional exchange-energy approximation with correct asymptotic  
13   behavior, *Phys. Rev. A.*, 38, 3098-3100, doi:10.1103/PhysRevA.38.3098, 1988.

14   Becker, S., Braatz, C., Lindner, J., and Tiemann, E.: Investigation of the predissociation of  
15   SO<sub>2</sub>: state selective detection of the SO and O fragments, *Chem. Phys.*, 196, 275-291,  
16   doi:10.1016/0301-0104(95)00114-4, 1995.

17   Bekki, S: Oxidation of volcanic SO<sub>2</sub>: a sink for stratospheric OH and H<sub>2</sub>O, *Geophys. Res.*  
18   *Lett.*, 22, 913-916, doi:10.1029/95GL00534, 1995.

19   Bekki, S. and Pyle, J. A.: A two-dimensional modeling study of the volcanic eruption of  
20   Mount Pinatubo, *J. Geophys. Res.*, 99, 18861-18869, doi:10.1029/94JD00667, 1994.

21   Black, G., Sharpless, R. L., and Slanger, T. G.: Rate coefficients at 298 K for SO reactions  
22   with O<sub>2</sub>, O<sub>3</sub>, and NO<sub>2</sub>, *Chem. Phys. Lett.*, 90, 55-58, doi:10.1016/0009-2614(82)83324-1,  
23   1982.

24   Bluth, G. J. S., Doiron, S. D., Schnetzler, C. C., Krueger, A. J., and Walter, L. S.: Global  
25   tracking of the SO<sub>2</sub> clouds from the June, 1991 Mount Pinatubo eruptions, *Geophys. Res.*  
26   *Lett.*, 19, 151-154, doi: 10.1029/91GL02792, 1992.

27   Canfield, D. E., Raiswell, R., Westrich, J. T., Reaves, C. M., and Berner, R. A.: The use of  
28   chromium reduction in the analysis of reduced inorganic sulfur in sediments and shales,  
29   *Chem. Geol.*, 54, 149-155, doi:10.1016/0009-2541(86)90078-1, 1986.

1 Castleman, A. W., Munkelwitch, H. R., and Manowitz, B.: Isotopic studies of the sulfur  
2 component of the stratospheric aerosol layer, Tellus, 26, 222-234, doi:10.1111/j.2153-  
3 3490.1974.tb01970.x, 1974.

4 Celani, P. and Werner H.-J.: Multireference perturbation theory for large restricted and  
5 selected active space reference wave functions, J. Chem. Phys., 112, 5546-5557, doi:  
6 10.1063/1.481132, 2000.

7 Cobos, C. J., Hippler, H., and Troe, J.: Falloff curves of the recombination reaction  $O + SO +$   
8  $M \rightarrow SO_2 + M$  in a variety of bath gases, J. Phys. Chem., 89, 1778-1783, doi:  
9 10.1021/j100255a048, 1985.

10 COESA (Committee on Extension to the Standard Atmosphere): U.S. Standard Atmosphere,  
11 1976, U. S. Government Printing Office, Washington, D. C., United States of America, 1976.

12 Chase, M. W., Davies, C. A., Downey, J. R., Frurip, D. J., McDonald, R. A., and Syverud, A.  
13 N.: NIST JANAF THERMOCHEMICAL TABLES 1985 Version 1.0, Standard Reference  
14 Data Program, National Institute of Standards and Technology, Gaithersburg, MD,  
15 <http://kinetics.nist.gov/janaf/>, 1986.

16 Chung, K., Calvert, J. G., and Bottenheim, J. W.: The photochemistry of sulfur dioxide  
17 excited within its first allowed band (3130 Å) and the “forbidden” band (3700-4000 Å), Int. J.  
18 Chem. Kinet., 7, 161-182, doi: 10.1002/kin.550070202, 1975.

19 Danielache, S. O., Eskebjerg, C., Johnson, M. S., Ueno, Y., and Yoshida, N.: High-precision  
20 spectroscopy of  $^{32}S$ ,  $^{33}S$ , and  $^{34}S$  sulfur dioxide: ultraviolet absorption cross sections and  
21 isotope effects, J. Geophys. Res. Atmos., 113, D17314, doi:10.1029/2007JD009695, 2008.

22 Danielache, S. O., Hattori, S., Johnson, M. S., Ueno, Y., Nanbu, S., and Yoshida,  
23 N.: Photoabsorption cross-section measurements of  $^{32}S$ ,  $^{33}S$ ,  $^{34}S$ , and  $^{36}S$  sulfur dioxide for the  
24  $B^1B_1-X^1A_1$  absorption band, J. Geophys. Res. Atmos., 117, D24301,  
25 doi:10.1029/2012JD017464, 2012.

26 Davis, D. D.: A kinetics review of atmospheric reactions involving  $H_xO_y$  compounds, Can. J.  
27 Chem., 52, 1405-1414, doi: 10.1139/v74-213, 1974.

28 DeMore, W. B., Sander, S. P., Golden, D. M., Hampson, R. F., Kurylo, M. J., Howard, C. J.,  
29 Ravishankara, A. R., Kolb, C. E., and Molina, M. J.: Chemical kinetics and photochemical

1 data for use in stratospheric modeling, evaluation number 12, JPL Publication 97-4, Jet  
2 Propulsion Laboratory, Pasadena, California, USA, 1997.

3 Dunning, T. H.: Gaussian basis sets for use in correlated molecular calculations. I. The atoms  
4 boron through neon and hydrogen, *J. Chem. Phys.*, 90, 1007-1023, doi:  
5 10.1063/1.456153, 1989.

6 Forrest, J. and Newman, L.: Silver-110 microgram sulfate analysis for the short time  
7 resolution of ambient levels of sulfur aerosol, *Anal. Chem.*, 49, 1579-1584,  
8 doi:10.1021/ac50019a030, 1977.

9 Freeman, D. E., Yoshino, K., Esmond, J. R., and Parkinson, W. H., High resolution  
10 absorption cross section measurements of SO<sub>2</sub> at 213 K in the wavelength region 172-240 nm,  
11 *Planet. Space Sci.*, 32, 1125-1134, doi: 10.1016/0032-0633(84)90139-9, 1984.

12 Frisch, M. J., Trucks, G. W., Schlegel, H. B., Scuseria, G. E., Robb, M. A., Cheeseman, J. R.,  
13 Scalmani, G., Barone, V., Mennucci, B., Petersson, G. A., Nakatsuji, H., Caricato, M., Li, X.,  
14 Hratchian, H. P., Izmaylov, A. F., Bloino, J., Zheng, G., Sonnenberg, J. L., Hada, M., Ehara,  
15 M., Toyota, K., Fukuda, R., Hasegawa, J., Ishida, M., Nakajima, T., Honda, Y., Kitao, O.,  
16 Nakai, H., Vreven, T., Montgomery, J. A., Jr.; Peralta, J. E., Ogliaro, F., Bearpark, M., Heyd,  
17 J. J., Brothers, E., Kudin, K. N., Staroverov, V. N., Kobayashi, R., Normand, J., Raghavachari,  
18 K., Rendell, A., Burant, J. C., Iyengar, S. S., Tomasi, J., Cossi, M., Rega, N., Millam, M. J.,  
19 Klene, M., Knox, J. E., Cross, J. B., Bakken, V., Adamo, C., Jaramillo, J., Gomperts,  
20 R., Stratmann, R. E., Yazyev, O., Austin, A. J., Cammi, R., Pomelli, C., Ochterski, J. W.,  
21 Martin, R. L., Morokuma, K., Zakrzewski, V. G., Voth, G. A., Salvador, P., Dannenberg, J. J.,  
22 Dapprich, S., Daniels, A. D., Farkas, Ö., Foresman, J. B., Ortiz, J. V., Cioslowski, J., Fox, D.  
23 J.: Gaussian 09, Gaussian, Inc., Wallingford, CT, <http://www.gaussian.com/>, 2009.

24 Gobbi, G. P., Congeduti, F., and Adriani, A.: Early stratospheric effects of the Pinatubo  
25 eruption, *Geophys. Res. Lett.*, 19, 997-1000, doi:10.1029/92GL01038, 1992.

26 Goodarzi, M., Vahedpour, M., and Nazari, F.: Theoretical study on the atmospheric formation  
27 of SO<sub>x</sub>(x = 1 - 3) in the SSO(<sup>1</sup>A') and O<sub>2</sub>(<sup>3</sup>Sigma\_g^-) reaction, *J. Molec. Struct. THEOCHEM*, 945,  
28 45-52, doi: 10.1016/j.theochem.2010.01.004, 2010.

29 Guo, S., Bluth, G. J. S., Rose, W. I., Watson, I. M., Prata, A. J.: Re-evaluation of SO<sub>2</sub> release  
30 of the 15 June 1991 Pinatubo eruption using ultraviolet and infrared satellite sensors,  
31 *Geochem. Geophys. Geosyst.*, 5, Q04001, doi:10.1029/2003GC000654, 2004.

1 Harris, E., Sinha, B., Hoppe, P., Crowley, J. N., Ono, S., and Foley, S.: Sulfur isotope  
2 fractionation during oxidation of sulfur dioxide: gas-phase oxidation by OH radicals and  
3 aqueous oxidation by  $\text{H}_2\text{O}_2$ ,  $\text{O}_3$ , and iron catalysis, *Atmos. Chem. Phys.*, 12, 407-424,  
4 doi:10.5194/acp-12-407-2012, 2012.

5 Harris, E., Sinha, B., Hoppe, P., and Ono, S.: High-precision measurements of  $^{33}\text{S}$  and  $^{34}\text{S}$   
6 fractionation during  $\text{SO}_2$  oxidation reveal causes of seasonality in  $\text{SO}_2$  and sulfate isotopic  
7 composition, *Environ. Sci. Tech.*, 47, 12174-12183, doi: 10.1021/es402824c, 2013.

8 Hattori, S., Schmidt, J., Johnson, M. S., Danielache, S. O., Yamada, A., Ueno, Y., and  
9 Yoshida, N.:  $\text{SO}_2$  photoexcitation mechanism links mass-independent sulfur isotopic  
10 fractionation in cryospheric sulfate to climate impacting volcanism, *Proc. Natl. Acad. Sci.*  
11 USA, 110, 17656-17661, doi:10.1073/pnas.1213153110, 2013.

12 Jou, S. H., Shen, M. Y., Yu, C. H., and Lee, Y. P.: Isomers of  $\text{SO}_3$ : infrared absorption of  
13 OSOO in solid argon, *J. Chem. Phys.*, 104, 5745-5753, doi:10.1063/1.471335, 1996.

14 Katagiri, H., Sako, T., Hishikawa, A., Yazaki, T., Onda, K., Yamanouchi, K., and Yoshino,  
15 K.: Experimental and theoretical exploration of photodissociation of  $\text{SO}_2$  via the  $\text{C}^1\text{B}_2$  state:  
16 identification of the dissociation pathway, *J. Molec. Struct.*, 413-414, 589-614, doi:  
17 10.1016/S0022-2860(97)00199-3, 1997.

18 Knizia, G., Adler, T. B., and Werner, H.-J.: Simplified CCSD(T)-F12 methods: theory and  
19 benchmarks, *J. Chem. Phys.*, 130, 054104, doi: 10.1063/1.3054300, 2009.

20 Knowles, P. J. and Werner, H.-J.: An efficient second-order MC SCF method for long  
21 configuration expansions, *Chem. Phys. Lett.*, 115, 259-267, doi: 10.1016/0009-  
22 2614(85)80025-7, 1985.

23 Knowles, P. J. and Werner, H.-J.: An efficient method for the evaluation of coupling  
24 coefficients in configuration interaction calculations, *Chem. Phys. Lett.*, 145, 514-522, doi:  
25 10.1016/0009-2614(88)87412-8, 1988.

26 Lanciki, A. L.: Discovery of sulfur mass-independent fractionation (MIF) anomaly of  
27 stratospheric volcanic eruptions in Greenland ice cores, Ph.D. thesis, South Dakota State  
28 University, Brookings, South Dakota, United States of America, 141 pp., 2010.

1 Lanciki, A., Cole-Dai, J., Thiemens, M. H., and Savarino, J.: Sulfur isotope evidence of little  
2 or no stratospheric impact by the 1783 Laki volcanic eruption, *Geophys. Res. Lett.*, 39,  
3 L01806, doi:10.1029/2011GL050075, 2012.

4 Lavigne, F., Degeai, J. P., Komorowski, J. C., Guillet, S., Robert, V., Lahitte, P.,  
5 Oppenheimer, C., Stoffel, M., Vidal, C. M., Surono, Pratomo, I., Wassmer, P., Hajdas, I.,  
6 Hadmoko, D. S., and Belizal, E.: Source of the great A.D. 1257 mystery eruption unveiled,  
7 Samalas volcano, Rinjani Volcanic Complex, Indonesia, *Proc. Natl. Acad. Sci. USA* (Early  
8 Edition), doi: 10.1073/pnas.1307520110, 2013.

9 Lee, C., Yang, W., and Parr, R. G., Development of the Colle-Salvetti correlation-energy  
10 formula into a functional of electron density, *Phys. Rev. B.*, 37, 785-789, doi:  
11 10.1103/PhysRevB.37.785, 1988.

12 Leung, F., Colussi, A. J., and Hoffmann, M. R.: Sulfur isotopic fractionation in the gas-phase  
13 oxidation of sulfur dioxide initiated by hydroxyl radicals, *J. Phys. Chem. A*, 105, 8073-8076,  
14 doi:10.1021/jp011014+, 2001.

15 Lévêque, C., Taïeb, R., and Köppel, H.: Communication: theoretical prediction of the  
16 importance of the  ${}^3\text{B}_2$  state in the dynamics of sulfur dioxide, *J. Chem. Phys.*, 140, 091101  
17 doi:10.1063/1.4867252, 2014.

18 Lyons, J. R.: Mass-independent fractionation of sulfur isotopes by isotope-selective  
19 photodissociation of  $\text{SO}_2$ , *Geophys. Res. Lett.*, 34, L22811, doi:10.1029/2007GL031031,  
20 2007.

21 Lyons, J. R.: Photolysis of long-lived predissociative molecules as a source of mass-  
22 independent isotope fractionation: the example of  $\text{SO}_2$ , *Adv. Quant. Chem.*, 55, 57-74, doi:  
23 10.1016/S0065-3276(07)00205-5, 2008.

24 Manatt, S. L. and Lane, A. L.: A compilation of the absorption cross-sections of  $\text{SO}_2$  from  
25 106 to 403 nm, *J. Quant. Spectrosc. Radiat. Transfer*, 50, 267 - 276, doi:10.1016/0022-  
26 4073(93)90077-U, 1993.

27 Martin, J. M. L.: Heat of atomization of sulfur trioxide,  $\text{SO}_3$ : a benchmark for computational  
28 thermochemistry, *Chem. Phys. Lett.*, 310, 271-276, doi: 10.1016/S0009-2614(99)00749-6,  
29 1999.

1 Masterson, A. L., Farquhar, J., and Wing, B. A.: Sulfur mass-independent fractionation  
2 patterns in the broadband UV photolysis of sulfur dioxide: pressure and third body effects,  
3 *Earth Planet. Sci. Lett.*, 306, 253-260, doi:10.1016/j.epsl.2011.04.004, 2011.

4 Molina, L. T. and Molina, M. J.: Absolute absorption cross sections of ozone in the 185- to  
5 350-nm wavelength range, *J. Geophys. Res. Atmos.*, 91, 14501-14501, doi:  
6 10.1029/JD091iD13p14501, 1986.

7 Oduro, H., KamyshnyJr, A., Guo, W., and Farquhar, J.: Multiple sulfur isotope analysis of  
8 volatile organic sulfur compounds and their sulfonium precursors in coastal marine  
9 environments, *Marine Chem.*, 124, 78-89, doi:10.1016/j.marchem.2010.12.004, 2011.

10 Ono, S., Whitehill, A. R., and Lyons, J. R.: Contribution of isotopologue self-shielding to  
11 sulfur mass-independent fractionation during sulfur dioxide photolysis, *J. Geophys. Res.*  
12 *Atmos.*, 118, 2444-2454, doi:10.1002/jgrd.50183, 2013.

13 Pavlov, A. A. and Kasting, J. F.: Mass-independent fractionation of sulfur isotopes in  
14 Archean sediments: Strong evidence for an anoxic Archean atmosphere. *Astrobiology*, 2, 27–  
15 41, doi:10.1089/153110702753621321, 2002.

16 Pavlov, A. A., Mills, M. J., and Toon, O. B.: Mystery of the volcanic mass-independent sulfur  
17 isotope fractionation signature in the Antarctic ice core, *Geophys. Res. Lett.*, 32, L12816,  
18 doi:10.1029/2005GL022784, 2005.

19 Phillips, L. F.: Absolute absorption cross sections for SO between 190 and 235 nm. *J. Phys.*  
20 *Chem.*, 85, 3994 – 4000, doi: 10.1021/j150626a009, 1981.

21 Ran, H., Xie, D., and Guo, H.: Theoretical studies of the C<sup>1</sup>B<sub>2</sub> absorption spectra of  
22 SO<sub>2</sub>isotopomers, *Chem. Phys. Lett.*, 439, 280-283, doi: 10.1016/j.cplett.2007.03.103, 2007.

23 Read, W. G., Froidevaux, L., and Waters, J. W.: Microwave limb sounder measurement of  
24 stratospheric SO<sub>2</sub> from the Mt. Pinatubo Volcano, *Geophys. Res. Lett.*, 20, 1299-1302, doi:  
25 10.1029/93GL00831, 1993.

26 Robock, A.: Volcanic eruptions and climate, *Rev. Geophys.*, 38(2), 191-219,  
27 doi:10.1029/1998RG000054, 2000.

28 Rottman, G. J., Woods, T. N., and McClintock, W.: SORCE solar UV irradiance results, *Adv.*  
29 *Space Res.*, 37, 201-208, doi: 10.1016/j.asr.2005.02.072, 2006.

1 Sander, S. P., Abbatt, J., Barker, J. R., Burkholder, J. B., Friedl, R. R., Golden, D. M., Huie,  
2 R. E., Kolb, C. E., Kurylo, M. J., Moortgat, G. K., Orkin, V. L., and Wine, P. H.: Chemical  
3 kinetics and photochemical data for use in atmospheric studies, evaluation no. 17, JPL  
4 Publication 10-6, Jet Propulsion Laboratory, Pasadena, California, USA,  
5 <http://jpldataeval.jpl.nasa.gov/>, 2011.

6 Savarino, J., Romero, J., Cole-Dai, J., Bekki, S., and Thiemens, M. H.: UV induced mass-  
7 independent sulfur isotope fractionation in stratospheric volcanic sulfate, *Geophys. Res. Lett.*,  
8 30, 2131, doi:10.1029/2003GL018134, 2003.

9 Schmidt, A., Thordarson, T., Oman, L. D., Robock, A., and Self, S.: Climatic impact of the  
10 long-lasting 1783 Laki eruption: inapplicability of mass-independent sulfur isotopic  
11 composition measurements, *J. Geophys. Res.*, 117, D23116, doi: 10.1029/2012JD018414,  
12 2012.

13 Schoeberl, M. R., Doiron, S. D., Lait, L. R., Newman, P. A., and Krueger, A. J.: A simulation  
14 of the Cerro Hudson SO<sub>2</sub> cloud, *J. Geophys. Res.*, 98, 2949-2955, doi:10.1029/92JD02517,  
15 1993.

16 Shemansky, D. E.: CO<sub>2</sub> extinction coefficient 1700-3000A, *J. Chem. Phys.*, 56, 1582, doi:  
17 10.1063/1.1677408, 1972.

18 Tanaka, N., Rye, D. M., Xiao, Y., and Lasaga, A. C.: Use of stable sulfur isotope systematics  
19 for evaluating oxidation reaction pathways and in-cloud scavenging of sulfur-dioxide in the  
20 atmosphere, *Geophys. Res. Lett.*, 21, 1519–1522, doi:10.1029/94GL00893, 1994.

21 Thordarson, T. and Self, S.: Atmospheric and environmental effects of the 1783-1784 Laki  
22 eruption: a review and reassessment, *J. Geophys. Res.*, 108, 4011,  
23 doi:10.1029/2001JD002042, 2003.

24 Tokue, I. and Nanbu, S.: Theoretical studies of absorption cross sections for the C<sup>1</sup>B<sub>2</sub>-X<sup>1</sup>A<sub>1</sub>  
25 system of sulfur dioxide and isotope effects, *J. Chm. Phys.*, 132, 024301, doi:  
26 10.1063/1.3277191, 2010.

27 Tsang, W. and Hampson, R. F.: Chemical kinetic database for combustion chemistry. Part I.  
28 Methane and related compounds. *J. Phys. Chem. Ref. Data*, 15, 1087 – 1279,  
29 doi:10.1063/1.555759, 1986.

1 Werner, H.-J., Knowles, P. J., Knizia, G., Manby, F. R., Schütz, M., Celani, P., Korona, T.,  
2 Lindh, R., Mitrushenkov, A., Rauhut, G., Shamasundar, K. R., Adler, T. B., Amos, R. D.,  
3 Bernhardsson, A., Berning, A., Cooper, D. L., Deegan, M. J. O., Dobbyn, A. J., Eckert, F., Goll,  
4 E., Hampel, C., Hesselmann, A., Hetzer, G., Hrenar, T., Jansen, G., Köppl, C., Liu, Y., Lloyd,  
5 A. W., Mata, R. A., May, A. J., McNicholas, S. J., Meyer, W., Mura, M. E., Nicklass, A.,  
6 O'Neill, D. P., Palmieri, P., Peng, D., Pflüger, K., Pitzer, R., Reiher, M., Shiozaki, T., Stoll, H.,  
7 Stone, A. J., Tarroni, R., Thorsteinsson, T., and Wang, M.: MOLPRO, version 2012.1, a  
8 package of ab initio programs, Cardiff, UK, <http://www.molpro.net>, 2012.

9 Westenberg, A. A. and Dehaas, N.: Rate of the O + SO<sub>3</sub> reaction, J. Chem. Phys., 62, 725-  
10 730, doi: 10.1063/1.430477, 1975.

11 Whitehill, A. R., and Ono, S.: Excitation band dependence of sulfur isotope mass-independent  
12 fractionation during photochemistry of sulfur dioxide using broadband light sources,  
13 Geochim. Cosmochim. Acta, 94, 238-253, doi:10.1016/j.gca.2012.06.014, 2012.

14 Whitehill, A. R., Xie, C., Hu, X., Xie, D., Guo, H., and Ono, S.: Vibronic origin of sulfur  
15 mass-independent isotope effect in photoexcitation of SO<sub>2</sub> at the implications to the early  
16 earth's atmosphere, Proc. Natl. Acad. Sci. USA, 110, 17697-17702,  
17 doi:10.1073/pnas.1306979110, 2013.

18 Xie, C., Hu, X., Zhou, L., Xie, D., and Guo, H.: *Ab initio* determination of potential energy  
19 surfaces for the first two UV absorption bands of SO<sub>2</sub>, J. Chem. Phys., 139, 014305, doi:  
20 10.1063/1.4811840, 2013.

21 Yoshino, K., Cheung, A. S. C., Esmond, J. R., Parkinson, W. H., Freeman, D. E., Guberman,  
22 S. L., Jenouvrier, A., Coquart, B., and Merienne, M. F.: Improved absorption cross-sections  
23 of oxygen in the wavelength region 205-240 nm of the Herzberg continuum, Planet. Space  
24 Sci., 36, 1469-1475, doi: 10.1016/0032-0633(88)90012-8, 1988.

25 Yoshino, K., Esmond, J. R., Cheung, A. S. C., Freeman, D. E., and Parkinson, W. H.: High  
26 resolution absorption cross sections in the transmission window of the Schumann-Runge  
27 bands and Herzberg continuum of O<sub>2</sub>, Planet. Space Sci., 40, 185-192, doi: 10.1016/0032-  
28 0633(92)90056-T, 1992.

29

1 Table 1. Summary of experiments performed

---

Experiment	Lamp	Filter	<i>T</i> / K	Bath Gas	Presented in
photolysis (temp.)	200 W D <sub>2</sub>	None	225 to 275	N <sub>2</sub>	Figures 2, 5; Table 2
photoexcitation (temp.)	150 W Xe	250 LP, H <sub>2</sub> O	225 to 275	N <sub>2</sub> /C <sub>2</sub> H <sub>2</sub>	Figure 2; Table 3
photolysis (added O <sub>2</sub> )	150 W Xe	None, 200 BP	298	N <sub>2</sub> /O <sub>2</sub>	Figures 3, 6; Tables 4, 5
photoexcitation (added O <sub>2</sub> )	150 W Xe	250 LP, 280 LP	298	N <sub>2</sub> /O <sub>2</sub>	Figure 3; Table 5

---

2

1 Table 2. Isotope ratios of elemental sulfur products from the SO<sub>2</sub> photolysis temperature  
2 experiments (Section 2.2)

<i>T</i> / K	$\delta^{33}\text{S}$ / ‰	$\delta^{34}\text{S}$ / ‰	$\delta^{36}\text{S}$ / ‰	$\Delta^{33}\text{S}$ / ‰	$\Delta^{36}\text{S}$ / ‰
225	103.05	191.16	349.12	8.02	-32.4
225	97.85	177.76	315.71	9.13	-35.8
250	87.19	161.31	288.97	6.61	-29.8
250	80.68	146.58	259.31	7.18	-28.9
275	72.16	132.59	236.37	5.57	-24.1
275	70.35	129.04	227.26	5.50	-25.5

3

1 Table 3. Isotope ratios of organosulfur products from the SO<sub>2</sub>photoexcitation temperature  
2 experiments (Section 2.2)

<i>T</i> / K	$\delta^{33}\text{S}$ / ‰	$\delta^{34}\text{S}$ / ‰	$\delta^{36}\text{S}$ / ‰	$\Delta^{33}\text{S}$ / ‰	$\Delta^{36}\text{S}$ / ‰
225	24.18	9.88	65.72	19.01	46.0
225	24.94	9.95	67.09	19.73	47.2
250	25.29	7.33	64.39	21.44	49.7
250	24.30	6.37	62.38	20.96	49.6
275	26.24	5.39	63.29	23.4	52.5
275	25.39	4.84	61.27	22.84	51.6

3

4

1 Table 4. Results from experiments of  $\text{SO}_2$  photolysis in the presence of varying amounts of  $\text{O}_2$   
 2 (Section 2.3) used to estimate  $k_{\text{R}6}$  (Sections 4.3 and 4.4).

Product	$p\text{O}_2 /$ kPa	Time / ks	Yield / $\mu\text{mol S}$	$\delta^{33}\text{S} /$ ‰	$\delta^{34}\text{S} /$ ‰	$\delta^{36}\text{S} /$ ‰	$\Delta^{33}\text{S} /$ ‰	$\Delta^{36}\text{S} /$ ‰	calculated $k_{\text{R}6} /$ $\text{cm}^6 \text{molecule}^{-2} \text{s}^{-1}$
$^*\text{S}^0 - 1$	0.00	21.6		74.00	129.68	220.54	8.63	-31.9	
$^*\text{S}^0 - 2$	0.00	21.6		78.42	137.52	232.90	9.18	-34.8	
$\text{S}^0\text{avg}$	0.00						8.91	-33.3	
$^*\text{SO}_3 - 1$	0.00	21.6	35.3	14.16	25.64	43.82	1.02	-5.2	
$^*\text{SO}_3 - 2$	0.00	21.6	28.9	11.51	21.14	36.21	0.67	-4.2	
$\text{SO}_3$	5.07	7.2	46.0	45.47	79.75	134.34	4.97	-19.5	$1.4 \times 10^{-37}$
$\text{SO}_3$	5.07	7.2	32.6	50.85	89.24	150.93	5.59	-21.6	$1.1 \times 10^{-37}$
$\text{SO}_3$	10.13	7.2	37.1	51.60	90.27	151.99	5.82	-22.5	$1.3 \times 10^{-37}$
$\text{SO}_3$	10.13	7.2	41.3	51.35	91.22	155.00	5.13	-21.5	$1.3 \times 10^{-37}$
$\text{SO}_3$	15.20	7.2	37.4	51.43	89.67	150.68	5.94	-22.6	$1.3 \times 10^{-37}$
$\text{SO}_3$	15.20	7.2	20.8	55.14	97.09	164.55	5.97	-23.4	$7.3 \times 10^{-38}$
$\text{SO}_3$	19.75	10.8	40.4	53.18	94.68	161.22	5.24	-22.2	$8.3 \times 10^{-38}$
$\text{SO}_3$	19.75	10.8	39.1	54.18	96.59	164.45	5.29	-22.7	$8.1 \times 10^{-38}$

3 \*  $\text{S}^0 - 1$  and  $\text{SO}_3 - 1$  are elemental sulfur and  $\text{SO}_3$  from the same experiment. Similarly,  $\text{S}^0 - 2$   
 4 and  $\text{SO}_3 - 2$  are elemental sulfur and  $\text{SO}_3$  from the same experiment.

5  
6

1 Table 5. Results from additional experiments of SO<sub>2</sub> photolysis in the presence of O<sub>2</sub> (Section  
 2 2.3). All results are from sulfate (SO<sub>3</sub>) product. Experiments were performed at a constant  
 3 total pressure of 101.3 kPa unless marked otherwise. Filter types are: 200 BP = 200 nm  
 4 bandpass filter, 250 LP = 250 nm longpass filter, 280 LP = 280 nm longpass filter.

Filter	$p\text{SO}_2 /$ Pa	$p\text{O}_2 /$ kPa	Flow / $\text{cm}^3 \text{s}^{-1}$	Time / ks	Yield / $\mu\text{mol S}$	$\delta^{33}\text{S} /$ ‰	$\delta^{34}\text{S} /$ ‰	$\delta^{36}\text{S} /$ ‰	$\Delta^{33}\text{S} /$ ‰	$\Delta^{36}\text{S} /$ ‰
none	314.0	19.00	16.67	1.8	62.3	38.45	67.23	117.84	4.22	-12.2
none	316.6	18.99	6.67	12.8	105.7	34.71	60.89	104.88	3.69	-12.5
none	50.7	20.06	1.67	18.0	70.9	32.91	58.18	95.36	3.26	-16.2
none	50.7	20.06	1.67	10.8	41.8	37.46	67.09	112.12	3.34	-17.0
none	25.2	20.16	1.68	18.0	40.8	22.80	40.08	64.63	2.31	-12.0
none	25.2	20.16	1.68	10.8	19.3	19.59	35.15	58.01	1.61	-9.2
*none	349.9	0.20	0.29	19.8	34.0	34.02	59.04	104.90	3.92	-9.2
200 BP	316.6	18.99	6.67	67.8	86.2	47.67	89.15	162.21	2.59	-11.9
200 BP	50.7	20.06	1.67	36.0	-	35.65	65.22	111.79	2.50	-14.0
250 LP	506.5	18.23	1.67	61.2	14.9	9.40	15.97	32.53	1.19	1.9
250 LP	506.5	18.23	1.67	61.2	1.9	19.56	33.12	68.70	2.60	4.5
280 LP	316.6	18.99	6.67	86.4	6.7	3.22	4.25	9.34	1.03	1.2

5 \* Experiment performed at 7.7 kPa total pressure to test low pressure limit

1 Table 6. Comparison of asymptotic energies of SO+O<sub>2</sub> obtained on the singlet and triplet  
 2 potential energy surfaces for SO<sub>3</sub> and those obtained by the sum of two separated species. All  
 3 energies are in kJ mole<sup>-1</sup> and are relative to the SO(<sup>3</sup>Σ<sup>-</sup>) + O<sub>2</sub>(<sup>3</sup>Σ<sub>g</sub><sup>-</sup>) calculated separately in  
 4 each ab-initio method.

	B3LYP	CASSCF	CASPT2//CASSCF	UCCSD(T)F12a//B3LYP
SO( <sup>3</sup> Σ <sup>-</sup> ) + O <sub>2</sub> ( <sup>3</sup> Σ <sub>g</sub> <sup>-</sup> )	0	0	0	0
(separated)				
SO( <sup>1</sup> Δ) + O <sub>2</sub> ( <sup>3</sup> Σ <sub>g</sub> <sup>-</sup> )				
(separated)	118.78	64.60	136.36	94.98
SO( <sup>3</sup> Σ <sup>-</sup> ) + O <sub>2</sub> ( <sup>1</sup> Δ <sub>g</sub> )				
(separated)	160.83	86.57	98.28	121.55
SO( <sup>1</sup> Δ) + O <sub>2</sub> ( <sup>1</sup> Δ <sub>g</sub> )				
(separated)	279.57	151.17	234.64	216.48
SO+O <sub>2</sub> (singlet)	279.57	0.00	-6.86	217.19
SO+O <sub>2</sub> (triplet)	27.61	0.00	-6.61	122.59

5  
 6

1 Table 7. Energies for stationary points on the singlet state potential energy surface at various  
 2 ab-initio levels. The energy is relative to the  $\text{SO}({}^3\Sigma^-) + \text{O}_2({}^3\Sigma_g^-)$  asymptote and zero point  
 3 energy is not included. All energies are given in kJ mole<sup>-1</sup>.

	B3LYP	CASSCF	CASPT2//CASSCF	UCCSD(T)F12a//B3LYP
$\text{SO}_3$	-287.73	-262.92	-348.69	-411.58
cyclic-OSOO	-60.17	-50.21	-101.75	-142.72
trans-OSOO	42.09	53.72	-18.87	-17.66
cis-OSOO	19.33	35.82	-31.42	-39.08
TS1: trans-to-cis	108.95	135.14	66.32	42.76
TS2: trans-to-cyclic	62.51	69.71	3.10	0.17
TS3: cis-to-cyclic	108.95	114.18	50.42	43.26
TS4: cyclic-to- $\text{SO}_3$	82.42	69.25	56.61	70.33
$\text{SO}({}^3\Sigma^-) + \text{O}_2({}^3\Sigma_g^-)$	0.00	0.00	0.00	0.00
$\text{SO}_2({}^1\text{A}_1) + \text{O}({}^1\text{D})$	292.04	159.28	206.27	152.84

4  
 5

1 Table 8. Energies for stationary points on the triplet state potential energy surface at various  
 2 ab-initio levels. The energy is relative to the  $\text{SO}({}^3\Sigma^-) + \text{O}_2({}^3\Sigma_g^-)$  asymptote and zero point  
 3 energy is not included. All energies are given in kJ mole<sup>-1</sup>.

	B3LYP	CASSCF	CASPT2//CASSCF	UCCSD(T)F12a//B3LYP
$\text{SO}_3$	136.02	293.21	115.90	75.14
cyclic-OSOO	-70.67	12.18	-105.06	-137.07
trans-OSOO	26.40	85.81	8.70	16.53
cis-OSOO	28.58	82.09	16.82	18.49
TS1: trans-to-cis	30.42	92.72	10.79	25.44
TS2: OSOO-to-				
cyclic	96.40	125.35	67.28	67.86
$\text{SO}_2 \dots \text{O}$	23.35	-71.34	-31.55	-58.28
TS3: cyclic-to-				
$\text{SO}_2 \dots \text{O}$	25.44	-62.93	-24.81	-54.06
$\text{SO}({}^3\Sigma^-) + \text{O}_2({}^3\Sigma_g^-)$	0.00	0.00	0.00	0.00
$\text{SO}_2({}^1\text{A}_1) + \text{O}({}^3\text{P})$	26.69	-55.44	13.64	-52.93

4

5

1 Table 9. Reactions and rate constants included in the kinetic model of the chemistry occurring  
 2 within reaction cell. Rate constants have units of  $s^{-1}$  for first order reactions,  $cm^3\ molecule^{-1}\ s^{-1}$   
 3  $^1$  for second order reactions (and effective second order reactions, denoted  $^2$ ), and  $cm^6$   
 4  $molecule^{-2}\ s^{-1}$  for third order reactions.

Reaction Number	Reaction	Rate constant	Reaction Order	Source
Photochemical Reactions				
1	$O_2 + h\nu \rightarrow O + O$	$1.0 \times 10^{-5}$	1	Yoshino et al. (1988, 1992)
2	$O_3 + h\nu \rightarrow O + O_2$	$5.7 \times 10^{-3}$	1	Molina and Molina (1986)
3	$O_3 + h\nu \rightarrow O(^1D) + O_2$	$1.0 \times 10^{-1}$	1	Molina and Molina (1986)
4	$H_2O_2 + h\nu \rightarrow OH + OH$	$1.7 \times 10^{-3}$	1	Sander et al. (2011)
5	$HO_2 + h\nu \rightarrow O(^1D) + OH$	$1.5 \times 10^{-2}$	1	Sander et al. (2011)
6	$SO_2 + h\nu \rightarrow SO + O$	$5.2 \times 10^{-3}$	1	Manatt and Lane (1993)
7	$SO + h\nu \rightarrow S + O$	$9.7 \times 10^{-3}$	1	Phillips (1981)
$O_x$ Chemistry				
8	$O + O + M \rightarrow O_2 + M$	$2.5 \times 10^{-14}$	$^2$	Tsang and Hampson (1986)
9	$O + O_2 + M \rightarrow O_3 + M$	$1.5 \times 10^{-14}$	$^2$	Sander et al. (2011)
10	$O + O_3 \rightarrow O_2 + O_2$	$8.0 \times 10^{-15}$	2	Sander et al. (2011)
$O(^1D)$ Chemistry				
11	$O(^1D) + O_2 \rightarrow O + O_2$	$4.0 \times 10^{-11}$	2	Sander et al. (2011)
12	$O(^1D) + O_3 \rightarrow O_2 + O_2$	$1.2 \times 10^{-10}$	2	Sander et al. (2011)
13	$O(^1D) + O_3 \rightarrow O + O + O_2$	$1.2 \times 10^{-10}$	2	Sander et al. (2011)
14	$O(^1D) + H_2 \rightarrow OH + H$	$1.2 \times 10^{-10}$	2	Sander et al. (2011)
15	$O(^1D) + H_2O \rightarrow OH + OH$	$2.0 \times 10^{-10}$	2	Sander et al. (2011)
16	$O(^1D) + N_2 \rightarrow O + N_2$	$3.1 \times 10^{-11}$	2	Sander et al. (2011)
17	$O(^1D) + SO_2 \rightarrow ?$	$2.2 \times 10^{-10}$	2	Sander et al. (2011)
$HO_x$ Chemistry				
18	$O + OH \rightarrow O_2 + H$	$3.3 \times 10^{-11}$	2	Sander et al. (2011)

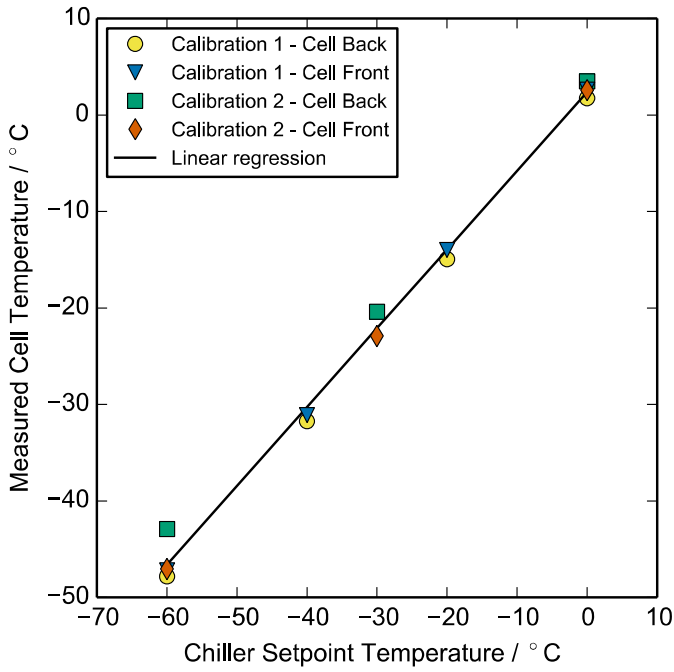
19	$O + HO_2 \rightarrow OH + O_2$	$5.9 \times 10^{-11}$	2	Sander et al. (2011)
20	$O + H_2O_2 \rightarrow OH + HO_2$	$1.8 \times 10^{-15}$	2	Sander et al. (2011)
21	$H + O_2 + M \rightarrow HO_2 + M$	$9.7 \times 10^{-13}$	*2	Sander et al. (2011)
22	$H + O_3 \rightarrow OH + O_2$	$2.9 \times 10^{-11}$	2	Sander et al. (2011)
23	$H + HO_2 \rightarrow OH + OH$	$7.2 \times 10^{-11}$	2	Sander et al. (2011)
24	$H + HO_2 \rightarrow O + H_2O$	$1.6 \times 10^{-12}$	2	Sander et al. (2011)
25	$H + HO_2 \rightarrow H_2 + O_2$	$6.9 \times 10^{-12}$	2	Sander et al. (2011)
26	$OH + O_3 \rightarrow HO_2 + O_2$	$7.3 \times 10^{-14}$	2	Sander et al. (2011)
27	$OH + H_2 \rightarrow H_2O + H$	$6.7 \times 10^{-15}$	2	Sander et al. (2011)
28	$OH + OH \rightarrow H_2O + O$	$1.8 \times 10^{-12}$	2	Sander et al. (2011)
29	$OH + OH + M \rightarrow H_2O_2 + M$	$6.4 \times 10^{-12}$	*2	Sander et al. (2011)
30	$OH + HO_2 \rightarrow H_2O + O_2$	$1.1 \times 10^{-10}$	2	Sander et al. (2011)
31	$OH + H_2O_2 \rightarrow H_2O + HO_2$	$1.8 \times 10^{-12}$	2	Sander et al. (2011)
32	$HO_2 + O_3 \rightarrow OH + O_2 + O_2$	$1.9 \times 10^{-15}$	2	Sander et al. (2011)
33	$HO_2 + HO_2(+M) \rightarrow H_2O_2 + O_2(+M)$	$2.6 \times 10^{-12}$	2 + *2	Sander et al. (2011)

#### SO<sub>x</sub> Chemistry

34	$O + SO_2 + M \rightarrow SO_3 + M$	$1.3 \times 10^{-11}$	*2	Sander et al. (2011)
35	$O_3 + SO_2 \rightarrow SO_3 + O_2$	$2.0 \times 10^{-22}$	2	Sander et al. (2011)
36	$OH + S \rightarrow H + SO$	$6.6 \times 10^{-11}$	2	Sander et al. (2011)
37	$OH + SO \rightarrow H + SO_2$	$8.3 \times 10^{-11}$	2	Sander et al. (2011)
38	$OH + SO_2 + M \rightarrow HOSO_2 + M$	$9.6 \times 10^{-13}$	*2	Sander et al. (2011)
39	$HO_2 + SO_2 \rightarrow OH + SO_3$	$1.0 \times 10^{-18}$	2	Sander et al. (2011)
40	$S + O_2 \rightarrow SO + O$	$2.3 \times 10^{-12}$	2	Sander et al. (2011)
41	$S + O_3 \rightarrow SO + O_2$	$1.2 \times 10^{-11}$	2	Sander et al. (2011)
42	$SO + O_2 \rightarrow SO_2 + O$	$8.0 \times 10^{-17}$	2	Sander et al. (2011)
43	$SO + O_2 + M \rightarrow SO_3 + M$	Varies	*2	Sander et al. (2011)

44	$\text{SO} + \text{O}_3 \rightarrow \text{SO}_2 + \text{O}_2$	$8.4 \times 10^{-14}$	2	Sander et al. (2011)
45	$\text{HOSO}_2 + \text{O}_2 \rightarrow \text{HO}_2 + \text{SO}_3$	$4.3 \times 10^{-13}$	2	Sander et al. (2011)
46	$\text{SO} + \text{HO}_2 \rightarrow \text{SO}_2 + \text{OH}$	$2.8 \times 10^{-11}$	2	DeMore et al. (1997)
47	$\text{SO} + \text{SO} \rightarrow \text{SO}_2 + \text{S}$	$8.3 \times 10^{-16}$	2	Chung et al. (1975)
48	$\text{SO} + \text{O} + \text{M} \rightarrow \text{SO}_2 + \text{M}$	$1.3 \times 10^{-11}$	*2	Cobos et al. (1985)
49	$\text{SO} + \text{SO}_3 \rightarrow \text{SO}_2 + \text{SO}_2$	$2.0 \times 10^{-15}$	2	Chung et al. (1975)
50	$\text{S} + \text{S} + \text{M} \rightarrow \text{S}_2 + \text{M}$	$7.5 \times 10^{-14}$	*2	Pavlov and Kasting (2002)
51	$\text{SO}_2 + 2 \text{ H}_2\text{O} \rightarrow \text{aerosol}$	$2.9 \times 10^{-31}$	3 (special)	Sander et al. (2011)
Other				
	k_out	Exit rate from cell	$2.1 \times 10^{-2}$	1

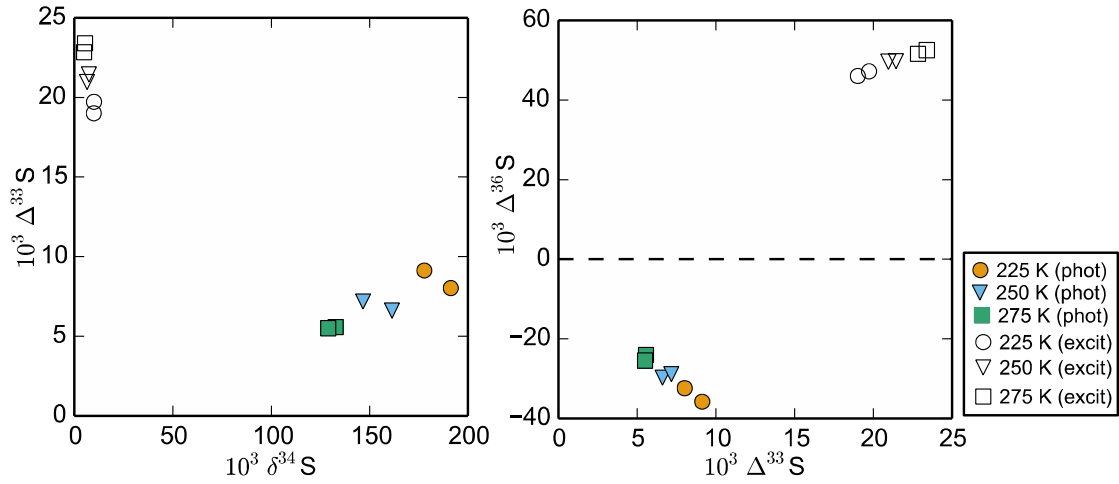
1      \* Effective second order reactions based on falloff curves for  $[\text{M}] = 2.5 \times 10^{19}$  and  $\text{M} = \text{N}_2, \text{O}_2$ . See sources for  
 2      additional information.  
 3  
 4



1

2 Figure 1. Results of the temperature calibration for the temperature controlled photochemical  
 3 reactor described in Section 2.1 The linear regression shown was used to calibrate the  
 4 temperature within the cell based on the setpoint temperature of the chiller. The regression  
 5 line is  $(T_{Cell} / ^\circ\text{C}) = 0.8160 \times (T_{Chiller} / ^\circ\text{C}) + 2.3514$ .

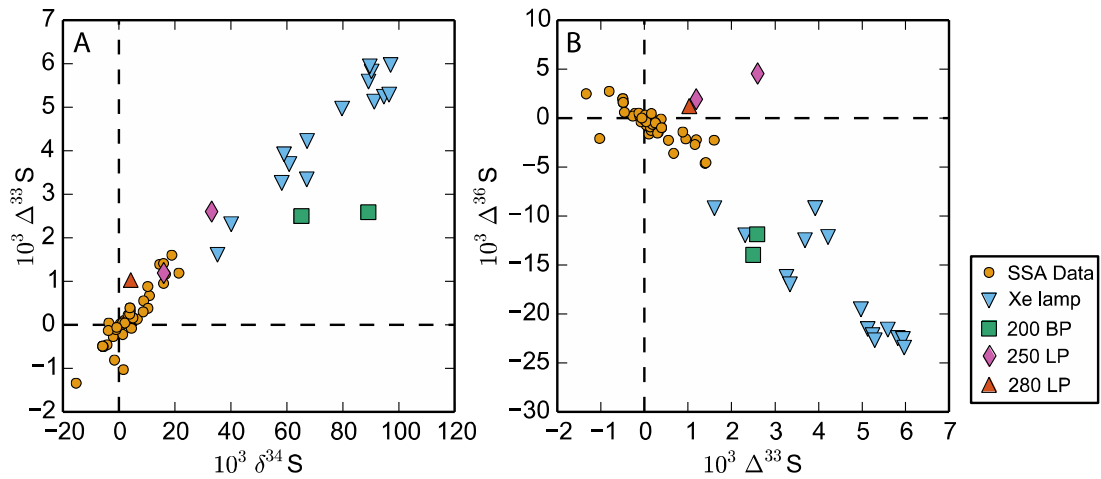
6



1

2 Figure 2. Results of the temperature experiments for  $\text{SO}_2$  photolysis and  $\text{SO}_2$  photoexcitation  
3 (Section 2.2). Results from  $\text{SO}_2$  photolysis experiments (phot) are shown in filled symbols  
4 and  $\text{SO}_2$  photoexcitation experiments (excit) are in empty symbols.

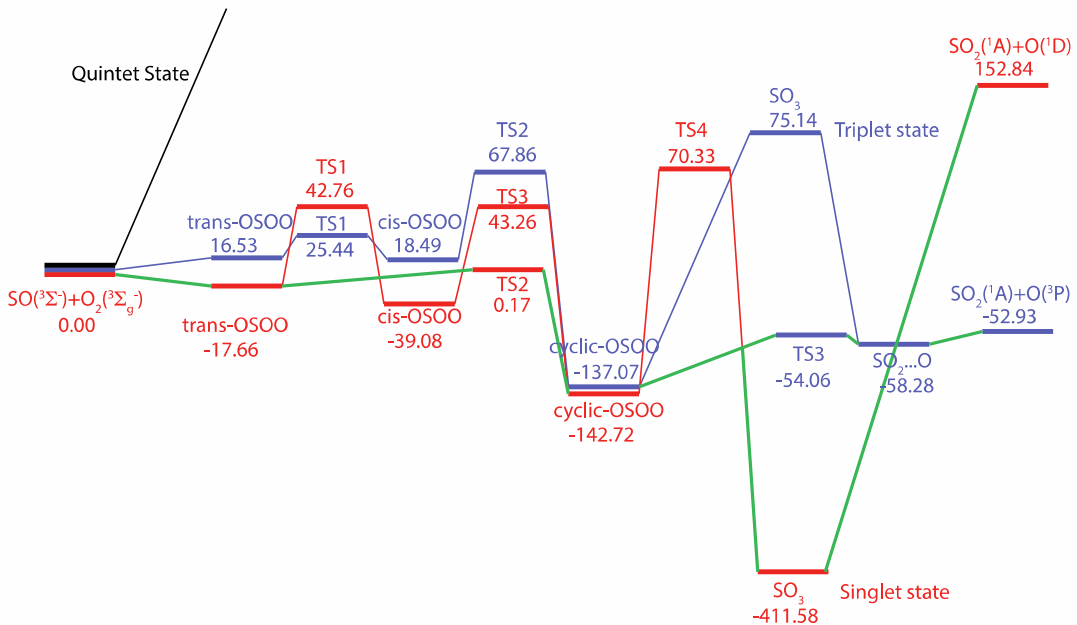
5



1

2 Figure 3. Isotopic results of the  $\text{SO}_2 + \text{O}_2$  experiments described in Section 2.3, compared with  
 3 stratospheric sulfate aerosol samples (SSA Data) from Savarino et al. (2003), Baroni et al.  
 4 (2007, 2008), Lanciki (2010), and Lanciki et al. (2012).

5

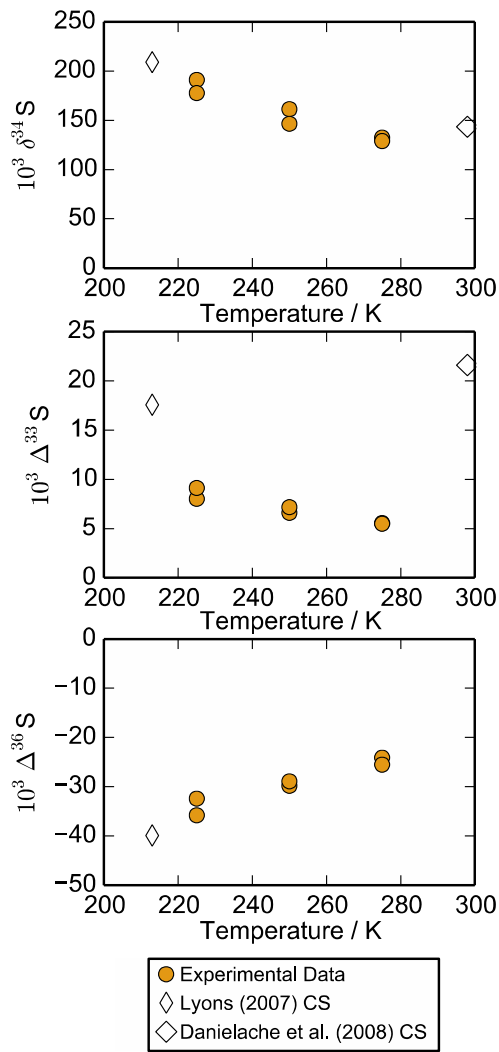


1

2 Figure 4. Potential energy profiles on the singlet (red) and triplet (blue) potential energy  
 3 surfaces for the  $\text{SO}_3$  system obtained using B3LYP optimization followed by UCCSD(T)-  
 4 F12a single point calculation, with the AVTZ basis set. The possible intersystem crossing  
 5 pathway is depicted by the solid green line. All energies are given in  $\text{kJ mol}^{-1}$  relative to the  
 6  $\text{SO}(^3\Sigma^-) + \text{O}_2(^3\Sigma_g^-)$  asymptote. The quintet (black) state is shown qualitatively due to its high  
 7 energy.

8

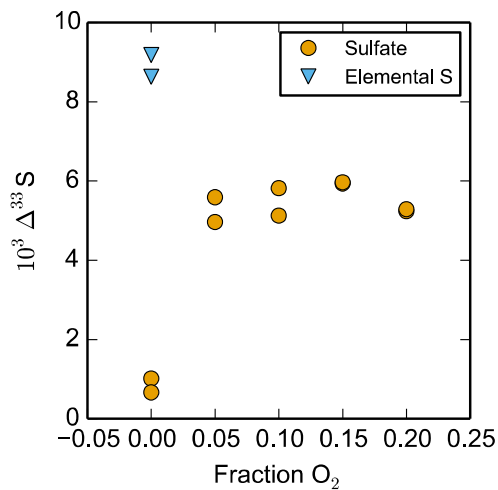
9



1

2 Figure 5. Comparison of  $\text{SO}_2$  photolysis temperature experiment results with predictions from  
3 isotopologue-specific absorption cross-sections (CS).

4

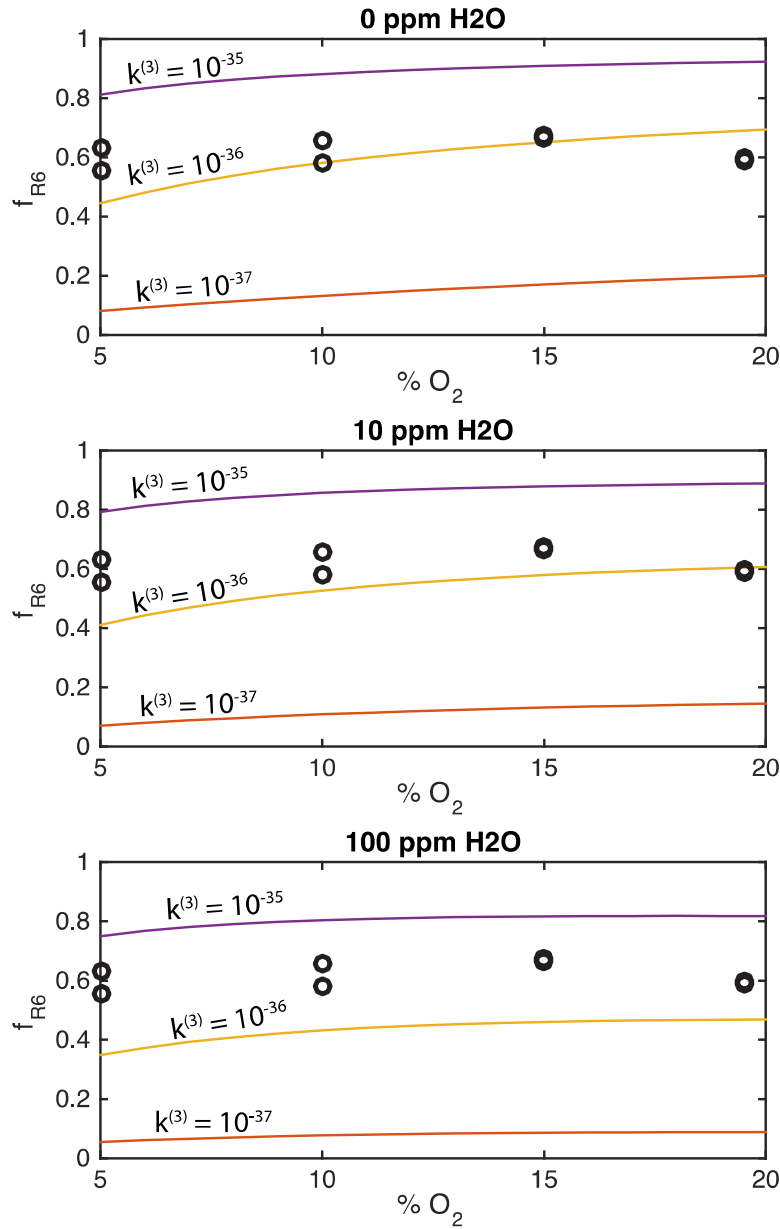


1

2 Figure 6.  $\Delta^{33}\text{S}$  values of sulfate from the photolysis of  $\text{SO}_2$  in the presence of  $\text{O}_2$  compared  
 3 with elemental sulfur and sulfate from  $\text{SO}_2$  photolysis in the absence of  $\text{O}_2$ . Conditions are  
 4 described in Section 4.3 and Table 4.

5

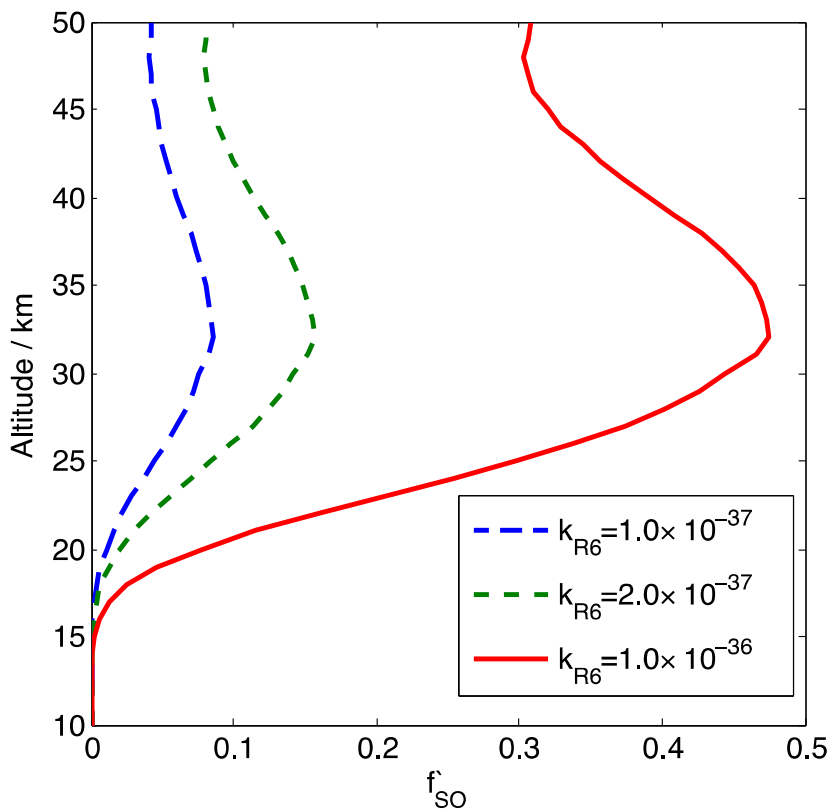
1



2

3 Figure 7. Results of kinetic model (Section 4.4, Table 9) compared to experimental data  
4 (circles) for  $f_{\text{R6}}$  (Equation 5) versus fraction of  $\text{SO}_3$  formed from R6 in the model. Contours on  
5 the plot are labeled with the value of rate constant  $k_{\text{R6}}$  input into the model for a given run.  
6 Experimental data is plotted as black circles. The model was run for three input values of  
7  $\text{H}_2\text{O}$  concentration: 0 ppmv (top), 10 ppmv (middle), and 100 ppmv (bottom).

8



1      Figure 8. Fraction of sulfate derived from reaction channel R6 ( $f_{SO}$ ) as a function of altitude for  
2      different values of  $k_{R6}$ .  
3  
4

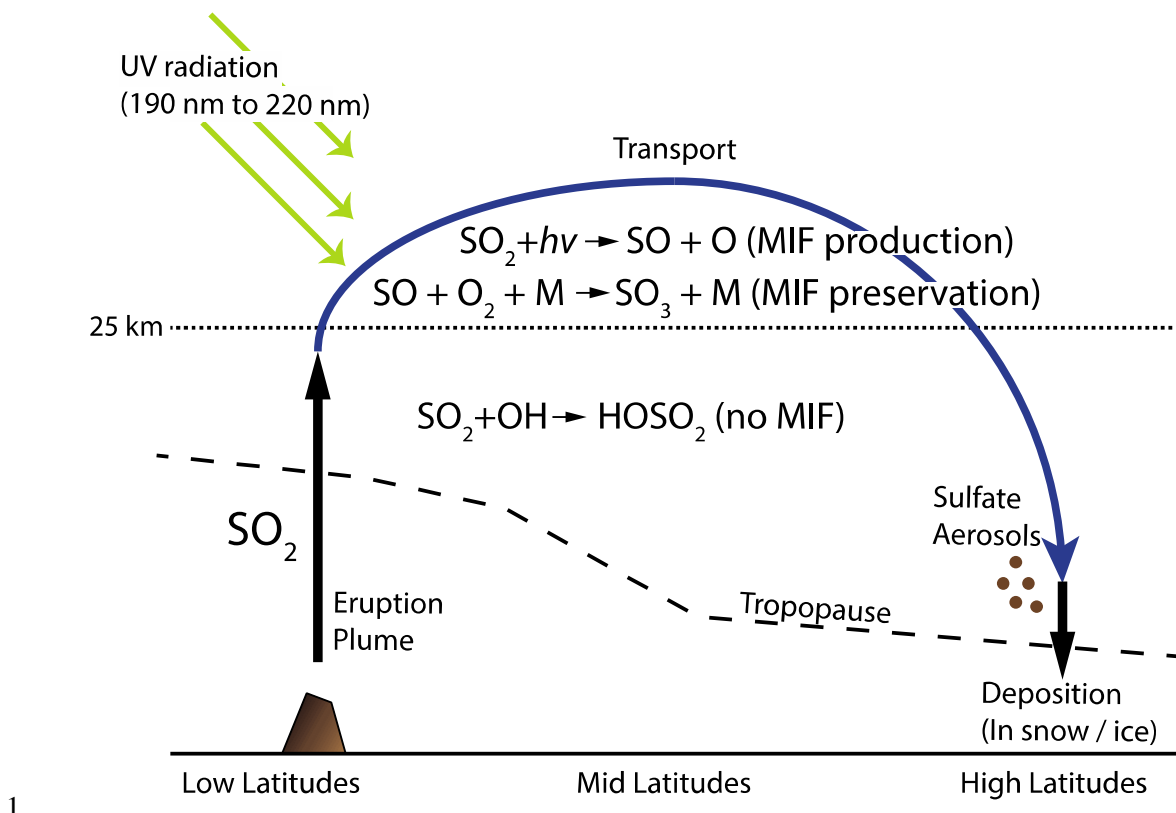


Figure 9. Schematic illustration of the production and preservation of mass-independent fractionation (MIF) in sulfur isotopes following explosive volcanic eruptions. Low latitude eruptions such as Pinatubo (1991) inject large amounts of  $\text{SO}_2$  into the stratosphere. Through stratospheric transport, it is brought to altitudes where  $\text{SO}_2$  photolysis can occur, producing large MIF signatures. The product of  $\text{SO}_2$  photolysis,  $\text{SO}$ , is preserved via termolecular reaction with  $\text{O}_2$ . The resulting  $\text{SO}_3$  forms sulfate aerosols, which are deposited at high latitudes in polar snow and ice core records.  $\text{SO}_2$  oxidation below around 25 km is dominantly by  $\text{OH}$ , which is a mass-dependent process.

10